

USE OF A HIGH-PURITY GERMANIUM SEMICONDUCTOR DETECTOR FOR
RAPID POST-NUCLEAR EVENT FORENSICS

A Thesis

by

STEVEN M. HOROWITZ

Submitted to the Office of Graduate and Professional Studies of
Texas A&M University
in partial fulfillment of the requirements for the degree of

MASTER OF SCIENCE

Chair of Committee,	William Charlton
Committee Members,	Craig Marianno
	Sunil Khatri

Head of Department,	Yassin Hassan
---------------------	---------------

August 2015

Major Subject: Nuclear Engineering

Copyright 2015 Steven M. Horowitz

ABSTRACT

This thesis investigates the ability of a high-purity germanium detector to perform post-detonation forensics on the debris from several types of nuclear weapons 24 hours after detonation. The ultimate result of this analysis would be the deployment of this detector on an autonomous robot for sample collection and remote analysis. Monte Carlo N-Particle Transport Code Version 6 (MCNP6) was utilized to simulate the detonation of five nuclear weapon loadings to a yield of 10 kilotons of TNT. Simulations included uranium weapons of 20%, 50%, and 90% enrichment, as well as reactor-grade and weapons-grade plutonium weapons. The resulting isotopics were assumed to be distributed evenly as fallout, and this fallout composition was utilized to generate a source term through the use of photon yield databases. A high-purity germanium detector was modeled in MCNP6. Using this model and the source term, the predicted response spectrum for each fallout composition was generated and compared using Genie spectroscopy software in an attempt to find differentiating features between them.

The ability to distinguish between fallout originating from a uranium or plutonium weapon was identified. If the ratio of photopeak count rates at 320 keV and 251 keV is near to or less than 0.05, the initial weapon loading was likely uranium. Once identified to be uranium, the count rate ratio of the 108 keV to the 251 keV photopeak can be utilized to determine a range for the initial uranium enrichment. The relative height of the 108 keV peak due to ^{239}Np changes drastically based on initial enrichment

due to differences in the production of ^{239}Np from neutron capture in ^{238}U and subsequent beta decay.

If the ratio of photopeak count rates at 320 keV and 251 keV is greater than 0.06, the initial weapon was likely plutonium. A methodology to distinguish between weapons-grade and reactor-grade plutonium was not identified. This is due to the similar fission yields of the plutonium isotopes, while yields of uranium and plutonium isotopes are sufficiently-different to allow for variations in the fallout spectra.

DEDICATION

To my friends and family.

ACKNOWLEDGEMENTS

I would like to give thanks to Dr. William Charlton for serving as my committee chair and my primary source of guidance throughout this project. Thank you to Dr. Craig Marianno and Dr. Sunil Khatri for serving as my committee members and support throughout this project. I would also like to give a special thanks Dr. Sunil Chirayath and Corey Keith for acting as sources of help outside of my committee. Thanks to Harvey Shepard and John LeJeune at Canberra who assisted me with obtaining the technical dimensions of the detector I was modeling.

I would like to thank all of the faculty in the nuclear engineering department at Texas A&M University for this opportunity and helping to make my graduate experience an enjoyable one. Studying at this school has been the greatest experience of my life. Without the assistance of the nuclear engineering faculty and administration, I would not have learned as much as I have or been as successful. Thanks to all of my fellow Aggies at Texas A&M University, where I finally feel at home.

I am extremely grateful to have had the support of my friends and family throughout this trying experience. Thank you to my mother and father, whose love and support sustained me throughout graduate school. Thank you to my friends, both new and old. To my girlfriend, thank you for keeping me sane throughout this process, and for your love and support. Finally, I am overwhelmingly grateful to have shared my graduate school experience with my best friends, Pablo and Aaron.

TABLE OF CONTENTS

	Page
ABSTRACT	ii
DEDICATION	iv
ACKNOWLEDGEMENTS	v
TABLE OF CONTENTS	vi
LIST OF FIGURES	viii
LIST OF TABLES	xi
1. INTRODUCTION AND LITERATURE REVIEW	1
1.1 Motivation	1
1.2 Objectives	1
1.3 Literature Review	11
2. SIMULATIONS	15
2.1 Modeling a Nuclear Detonation in MCNP6	15
2.2 Modeling a Post-Detonation Environment with an HPGe Detector	20
3. ANALYSIS IN GENIE	33
3.1 VMS Standard Peak Search	33
3.2 Energy Group 1	34
3.3 Energy Group 2	41
3.4 Energy Group 3	46
3.5 Energy Group 4	49
3.6 Other Spectral Features	51
3.7 Issues with Differentiating Reactor-Grade and Weapons-Grade Plutonium	53
3.8 Determination of Initial Weapon Loading: A Flowchart	56
4. CONCLUSIONS	58
4.1 Future Work	58
4.2 Sources of Error	59
REFERENCES	63

APPENDIX A FISSION PRODUCTS TRACKED IN MCNP6.....	66
APPENDIX B RELATIVE ERRORS FOR PHOTON SPECTRA.....	67
APPENDIX C ADDITIONAL FISSION YIELD DATA	70
APPENDIX D MCNP6 BURNUP DECK FOR 20%-ENRICHED URANIUM	71
APPENDIX E MCNP6 INPUT DECK FOR A 20%-ENRICHED URANIUM FALLOUT PHOTON SOURCE WITH DETECTOR	76

LIST OF FIGURES

	Page
Figure 1. Photoelectric absorption.	3
Figure 2. Compton scattering.	3
Figure 3. Photon spectrum displaying various features on an intermediate-sized detector.	5
Figure 4. Diagram displaying the difference between the bandgaps of insulators and semiconductors.	6
Figure 5. Reverse-bias p-n junction.	9
Figure 6. Multiplication factors for each weapon for each burnup step.	18
Figure 7. Side-view of the germanium crystal for the GL0515R HPGe detector with dimensions in units of mm.....	22
Figure 8. MCNP6 model of germanium crystal, aluminum window, and soil sample plotted in Xming.....	24
Figure 9. Overall problem geometry in MCNP6 plotted in Xming.	25
Figure 10. Photon spectrum on an HPGe detector simulated in MCNP6 24 hours after the detonation of a 10-kiloton weapon fueled with 20%-enriched uranium.	29
Figure 11. Photon spectrum on an HPGe detector simulated in MCNP6 24 hours after the detonation of a 10-kiloton weapon fueled with 50%-enriched uranium.	30
Figure 12. Photon spectrum on an HPGe detector simulated in MCNP6 24 hours after the detonation of a 10-kiloton weapon fueled with 90%-enriched uranium.	31
Figure 13. Photon spectrum on an HPGe detector simulated in MCNP6 24 hours after the detonation of a 10-kiloton weapon fueled with reactor-grade plutonium.	32
Figure 14. Photon spectrum on an HPGe detector simulated in MCNP6 24 hours after the detonation of a 10-kiloton weapon fueled with weapons-grade plutonium.	32

Figure 15. Peaks identified in Genie for the first analyzed energy group of the 20%-enriched uranium fallout spectrum.	35
Figure 16. Peaks identified in Genie for the first analyzed energy group of the 50%-enriched uranium fallout spectrum.	35
Figure 17. Peaks identified in Genie for the first analyzed energy group of the 90%-enriched uranium fallout spectrum.	36
Figure 18. Initial uranium enrichment versus the ratio of the 108 keV to the 251 keV peak count rates.....	38
Figure 19. Peaks identified in Genie for the first analyzed energy group of the reactor-grade plutonium fallout spectrum.	39
Figure 20. Peaks identified in Genie for the first analyzed energy group of the weapons-grade plutonium fallout spectrum.....	40
Figure 21. Initial uranium enrichment versus the ratio of the 320 keV to the 251 keV peak count rates.....	41
Figure 22. Peaks identified in Genie for the second analyzed energy group of the 20%-enriched uranium fallout spectrum.	42
Figure 23. Peaks identified in Genie for the second analyzed energy group of the 50%-enriched uranium fallout spectrum.	42
Figure 24. Peaks identified in Genie for the second analyzed energy group of the 90%-enriched uranium fallout spectrum.	43
Figure 25. Peaks identified in Genie for the second analyzed energy group of the reactor-grade plutonium fallout spectrum.	44
Figure 26. Peaks identified in Genie for the second analyzed energy group of the weapons-grade plutonium fallout spectrum.....	44
Figure 27. Peaks identified in Genie for the third analyzed energy group of the 20%-enriched uranium fallout spectrum.	46
Figure 28. Peaks identified in Genie for the third analyzed energy group of the 50%-enriched uranium fallout spectrum.	47
Figure 29. Peaks identified in Genie for the third analyzed energy group of the 90%-enriched uranium fallout spectrum.	47

Figure 30. Peaks identified in Genie for the third analyzed energy group of the reactor-grade plutonium fallout spectrum.	48
Figure 31. Peaks identified in Genie for the third analyzed energy group of the weapons-grade plutonium fallout spectrum.....	49
Figure 32. Peaks identified in Genie for the fourth analyzed energy group of the reactor-grade plutonium fallout spectrum.	50
Figure 33. Peaks identified in Genie for the fourth analyzed energy group of the weapons-grade plutonium fallout spectrum.....	50
Figure 34. Fission yield data for ^{235}U and ^{238}U for 500 keV neutrons.	53
Figure 35. Fission yield data for ^{239}Pu and ^{240}Pu for 500 keV neutrons.	55
Figure 36. Fission yield data for ^{239}Pu and ^{241}Pu for 500 keV neutrons.	55
Figure 37. Fission yield data for ^{239}Pu and ^{235}U for 500 keV neutrons.....	56
Figure 38. Flowchart to determine initial fissile material content. All ratio values are approximate.	57
Figure 39. Relative errors for the 20%-enriched uranium spectra.	67
Figure 40. Relative errors for the 50%-enriched uranium spectra.	67
Figure 41. Relative errors for the 90%-enriched uranium spectra.	68
Figure 42. Relative errors for the reactor-grade plutonium fallout spectra.....	68
Figure 43. Relative errors for the weapons-grade plutonium fallout spectra.....	69
Figure 44. Fission yield data for ^{238}Pu and ^{239}Pu for 500 keV neutrons.	70
Figure 45. Fission yield data for ^{239}Pu and ^{242}Pu for 500 keV neutrons.	70

LIST OF TABLES

	Page
Table 1. Isotopics of the plutonium weapons to be investigated in this project.....	16
Table 2. Number of fissions per second for various isotopes in each weapon for the first corrector step.	20
Table 3. Average neutron energy causing fission.	20
Table 4. Germanium crystal and window properties for the GL0515R HPGe detector.	21
Table 5. Values utilized to find the GEB parameters.....	23
Table 6. Composition of air to be used in MCNP.	27
Table 7. Composition of soil to be used in MCNP.	27
Table 8. Analysis of 108 keV and 251 keV peaks to determine initial uranium enrichment in the weapon.	37
Table 9. Analysis of 320 keV and 251 keV peaks to differentiate a uranium weapon from a plutonium weapon.	41
Table 10. Analysis of 498 keV and 837 keV peaks to differentiate between uranium and plutonium fallout.	45
Table 11. Peaks with the largest percent differences for reactor-grade and weapons-grade plutonium.....	51
Table 12. Tier-3 fission products tracked in MCNP6.	66

1. INTRODUCTION AND LITERATURE REVIEW

1.1 Motivation

The use of prompt diagnostics following the detonation of a nuclear weapon is crucial in order to make decisions of appropriate ensuing actions, including, for instance, a retaliatory response. Forensic scientists must be able to analyze certain material and radiological characteristics of the fallout at the detonation site in order to extract from this data information about where the weapon may have originated and where it likely had not originated. It is desired that radiation samples be able to be acquired within 24 hours following the event so that appropriate measures be taken in order to restore national security. Post-detonation environments have dangerously-high radiation levels which are inaccessible to human beings. Therefore, it is prudent to employ robotic and remote systems in order to acquire necessary data and samples. While such robotic systems do exist, these systems do not have “on-the-fly” analysis capability which will be necessary following a nuclear catastrophe.

1.2 Objectives

One such method of rapidly-analyzing a radiological sample is the utilization of gamma-ray spectroscopy. This involves employment of a radiation detector such as a scintillation detector or semiconductor detector to observe the frequency distribution of the energies of the photon emissions from a sample. By analyzing the energies and heights of certain peaks, radiological information of the sample can be obtained which can be used to infer information about the original weapon. One important characteristic

of detector performance is its resolution, which describes how close two photons can be in energy while still remaining distinguishable. In a post-detonation environment, many different fission products make the need for high resolution critical, since the emitted photons are within close proximity to each other. Therefore, it is suggested that a high-purity germanium (HPGe) detector (likely mechanically-cooled) be employed to distinguish peaks. It is proposed that a photon spectrum can be obtained on soil samples in the post-detonation area, rapidly analyzed in the field through a remotely-operated robotic system, and basic forensics information of the weapon be able to be conveyed through obtained data. This information will then be presented to personnel in national intelligence agencies so that an appropriate response can be made.

1.2.1 Photon Spectroscopy

Photon spectroscopy describes the process of analyzing a plot of the frequency of photon emissions from a photon-emitting material to determine radiological properties of the constituents of the material.¹ X-rays and gamma rays interact primarily through photoelectric absorption, Compton scattering, and pair production reactions.¹ When the total energy of the incident photon is desired, the user would seek a full-energy photopeak within the spectrum where the photon deposits all of its initial energy. The common way for this to occur is photoelectric absorption. In this interaction, the incident photon transfers its initial energy to an orbital electron, which is ejected with kinetic energy equal to the photon's initial energy minus the binding energy of the electron, E_b . The photon's kinetic energy is given by $h\nu$, where h is Planck's constant and ν is its frequency.¹ An electron vacancy results, causing the atom to emit a characteristic X-ray

or Auger electron. Although this X-ray can escape, it typically is absorbed in the detector due to its low energy, resulting in the total absorption of the photon's initial energy.¹ The photoelectric absorption process is displayed in Figure 1.

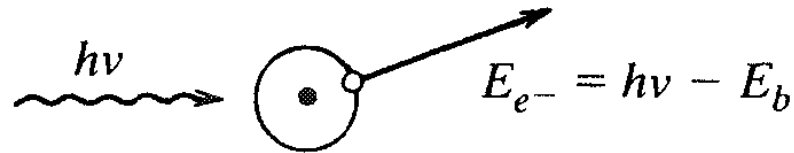


Figure 1. Photoelectric absorption.¹

Compton scattering describes the collision of a gamma-ray photon with an electron which is assumed to be unbound. The resulting photon and electron receive energies as a function of the scattering angle. This process is displayed in Figure 2.



Figure 2. Compton scattering.¹

The energy of the recoil electron is given by

$$E_{e^-} = h\nu \frac{\frac{h\nu}{mc^2}(1 - \cos\theta)}{1 + \frac{h\nu}{mc^2}(1 - \cos\theta)} \quad (1)$$

where θ is the scattering angle displayed in Figure 2, m is the rest mass of an electron, and c is the speed of light in a vacuum.¹ Since all scattering angles can occur in a detector, this results in a continuum of possible energies which can be transferred ranging from 0 to the maximum energy transferrable in a head-on collision called the Compton edge. This distribution of possible deposited energies is called a Compton continuum.¹ Multiple Compton scatters can result in what is known as a Compton valley, which is below the photopeak energy and above the energy of the Compton edge.¹

The third type of major photon interaction is pair production, in which a photon disappears and creates an electron-positron pair.¹ The photon must have a minimum energy of 1.022 MeV, equal to the rest mass of the pair, for this reaction to occur. Excess energy is shared as kinetic energy by the two emergent particles. The electron and positron deposit all of their kinetic energy into the medium within several millimeters. Once it slows down, the positron then annihilates with an electron in the medium, resulting in two 0.511 MeV gamma rays traveling in opposite directions to conserve momentum.¹ Since the detector has a finite size, there is a probability these photons can escape the detector. If both of these annihilation photons escape, this results in a double escape peak 1.022 MeV below the photopeak, while if only a single photon escapes, this results in a single escape peak 0.511 MeV below the photopeak energy.¹ A basic spectrum from an intermediate-sized detector with no surrounding material from a

photon source with energies greater than 1.022 MeV is shown in Figure 3.¹ This figure also ignores characteristic X-rays from any surrounding material, the backscatter peak, and an annihilation peak since it assumes there are no surrounding materials or shielding or that these are sufficiently far away to be neglected.

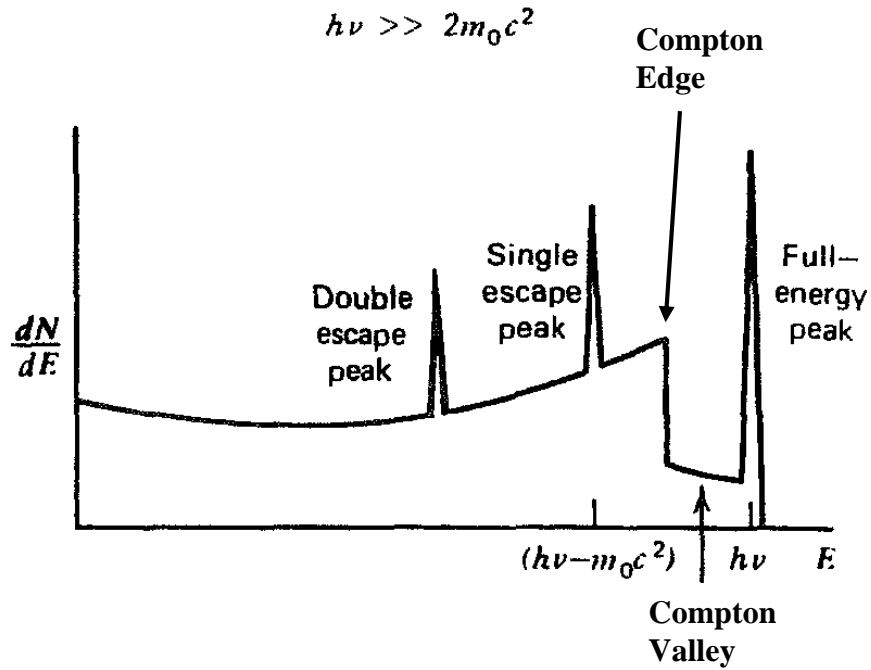


Figure 3. Photon spectrum displaying various features on an intermediate-sized detector.¹

1.2.2 High-Purity Germanium Detectors

Germanium is a semiconductor, which is a type of material with electron conductivity between that of conductors and insulators.¹ Crystalline materials have a periodic lattice which forms discrete energy bands within the material in which its

electrons must exist. The lower band contains outer-shell electrons which are bound to lattice sites within the material, and is called a valence band.¹ The conduction band contains electrons which are free to migrate throughout the material.¹ These two bands are separated by a bandgap. It is the size of this bandgap which determines the classification of the material as either a conductor, semiconductor, or insulator. Figure 4 displays the simplified diagram of the differences between the bandgaps of insulators and semiconductors.

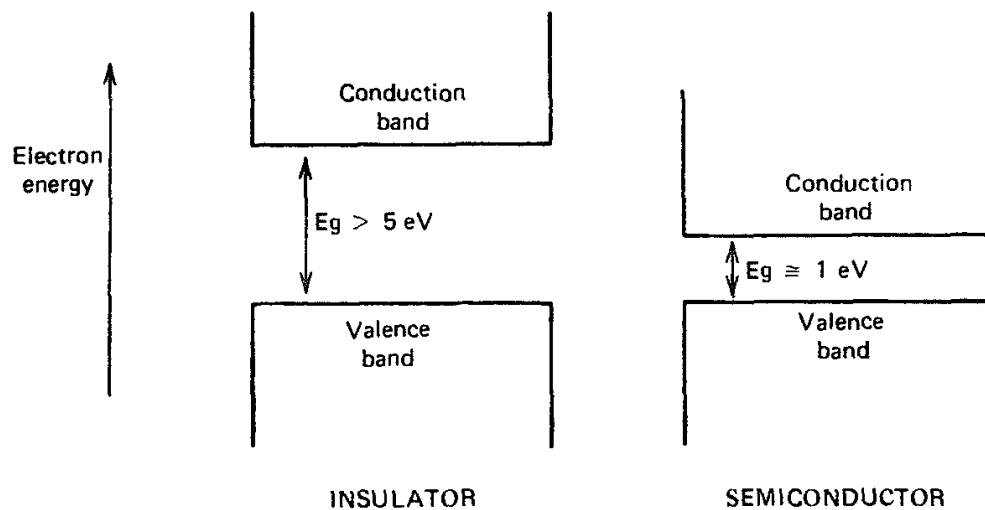


Figure 4. Diagram displaying the difference between the bandgaps of insulators and semiconductors.¹

Metals are conductors, such as copper, and have electrons in the conduction band that are free to move throughout the material. Insulators such as glass have electrons in the valence band that are bound to individual atoms. In comparison, semiconductors have electrons that are initially bound to individual atoms, but if excited can jump from

the valance band to the conduction band and therefore be free to travel throughout the material.¹ When radiation passes through a semiconductor, valance electrons are excited. Depending on the amount of excitation and the value of the bandgap, the excited electrons can move from the valance band to the conduction band. This results in an additional electron in the conduction band and a vacancy in the valance band, which is known as an electron-hole pair. These electron-hole pairs are referred to as charge carriers. Under the influence of an electric field, the charge-carriers migrate and collect producing an output signal.¹

Semiconductor detectors often use doping to lower the required band gap and improve the conductivity of the material. Doping is the process of introducing impurities within the crystal structure of the material. There are two basic types of doping, n-type (donor impurities) and p-type (acceptor impurities).¹ Donor impurities have an extra electron that is not bound and therefore is easy to dislodge. This lowers the required energy for the electron to jump from the valance band to the conduction band. This shifts the equilibrium between electrons and holes in favor of the number of free electrons, so that the hole concentration plays a very small role in determining the electrical conductivity of the material. Electrons are the majority carriers and holes are minority carriers.¹ In p-type doping, the acceptor impurity atoms have one fewer valence electrons than the surrounding atoms. This results in an unsaturated covalent bond, representing a hole. These create sites within the band gap to which electrons can move. Holes are the majority carrier for p-type doping and control the electrical conductivity.¹

Many HPGe detectors, including the one used in this project, use what is known as a p-n junction, which has p-type impurities on one end and n-type impurities on the other end. When a p-n junction is formed, free electrons on the n-side and free holes on the p-side can move across the junction and cancel each other out. This leaves positive ions near the n-side and negative ions near the p-side that are uncompensated. This results in a center region that is depleted of moving charge, which inhibits further transfer.¹ Due to this reduction of charge carriers, any charge carriers created by an ionizing particle are easily detected. The size of the depletion region can be increased by applying a reverse bias to the p-n junction. In a reverse bias, the negative terminal on the p-side attracts positive holes and the positive terminal on the n-side attracts the negative electrons. This removes additional carriers from the depletion region. If the concentrations of the donor impurities are equal on both sides, the depletion region will extend equally into both sides of the detector.¹ The resulting electric field quickly sweeps impurities caused by radiation or thermal excitation out of the depletion region within a few nanoseconds, resulting in very favorable timing characteristics. This reverse-bias p-n junction is shown in Figure 5.

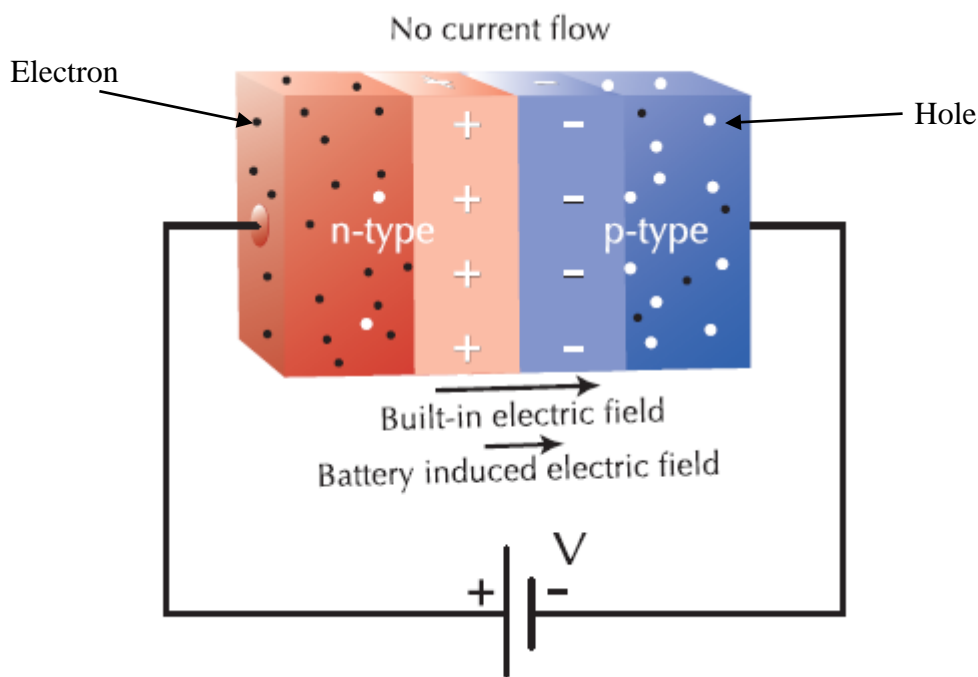


Figure 5. Reverse-bias p-n junction.²

The reverse biasing in HPGe detectors can cause what is known as a dead layer. This represents a thin layer on the crystal's surface in which radiation interactions are not detected.¹ Radiation must traverse this dead layer to enter into the active portion of the crystal. This dead layer is typically very small, and the presence of it is usually negligible for photons above approximately 200 keV.¹ However, for photons with lower energies such as X-rays, this dead layer must be accounted for.

HPGe detectors have excellent energy resolution due to the large number of information carriers produced per amount of incident radiation energy relative to other semiconductor detectors.¹ The detector is very sensitive to incoming radiation and therefore is usually the preferred detector for gamma-ray spectroscopy when resolution

is crucial. A typical method of describing the resolution of a radiation detector is to define its full-width at half-maximum (FWHM) for a specific photopeak. The FWHM defines the width of a photopeak in units of energy or channels at half of the maximum height of the peak.¹ A typical FWHM value for an HPGe detector is on the order of several keV, compared to several tens of keV for other semiconductors such as cadmium-zinc-telluride (CdZnTe) and various scintillation detectors.¹ For nuclear forensics applications, high resolution is crucial to the determination of material properties. In radioactive fallout, the close proximity in energy of many of the emitted photons induces the need for high-resolution detection systems.

1.2.3 Monte Carlo N-Particle Transport Code

Monte Carlo methods were developed by scientists at Los Alamos during the development of nuclear weapons in the 1940's, and simply describe the utilization of probability and outcome to study the behavior of various phenomena.³ Since the transport of radiation can be assumed to be a stochastic process, the Monte-Carlo N-Particle (MCNP) radiation transport code developed by Los Alamos National Laboratory uses probability distributions to predict the behavior of particles in nuclear systems.⁴ MCNP allows the user to define the desired geometry, particle source location and type, material constituents, the types of results produced, and the cross sections to be used in the transport problem.

MCNP variance reduction techniques allow the user to more rapidly obtain statistically-sound results while maintaining the integrity of the problem.⁵ This is done by sampling probability distributions to bias the traveling particles to reach the tally. In

source biasing, the source is sampled such that the particles are preferentially emitted in a manner that will contribute towards the tallies in the problem. In order to compensate for the bias, the weight of each particle is decreased as a function of the amount of biasing which is implemented.⁵

MCNP Version 6 (MCNP6) performs burnup and depletion calculations by communication with the embedded code CINDER90. First, MCNP6 reads in the parameters of the problem and performs steady-state calculations to calculate the eigenvalue, group fluxes, and energy-integrated reaction rates. It then delivers these parameters to CINDER90 which performs a depletion calculation to the halfway point of the first given time step. This first burnup calculation to the halfway point of the time step is called the predictor step. The new nuclide concentrations at the halfway point are then used within MCNP6 to calculate a revised set of group fluxes and energy-integrated reaction rates. These adjusted values for group fluxes and reaction rates at the halfway point are assumed to be the average values for the burn step, and are used to perform the burnup calculation for the entire step. This calculation is called the corrector step. The updated fluxes and number densities are then fed into the next time step, where the entire process is repeated. This process is called the predictor-corrector method, and it is repeated for the number of time steps requested in the problem.⁶

1.3 Literature Review

1.3.1 Unmanned Robotic Vehicles for Nuclear Events

Most literature on the use of autonomous vehicles concerns the application of mapping the radiation sources within the environment and disregards forensics analysis,

specifically a rapid in-the-field forensics analysis.^{7,8} In a study by Towler et al., a sodium-iodide scintillation crystal was placed on an autonomous helicopter for the purposes of radiation mapping. This effort focused strictly on contour mapping of the radiation levels and did not concern source identification.⁹ In several similar publications by Pöllänen et al., an unmanned aerial vehicle (UAV) was able to collect air samples for alpha particles as well as utilize a cesium-iodide scintillation crystal.^{10,11} Although sources of the alpha particles were identified, the alpha particle analysis had to be completed on the samples in a moving laboratory, therefore not an “in-the-field” analysis.

Furthermore, the papers did not address source identification using the spectrometer with an associated spectral analysis, only source location and minimal detectable activity of various photon sources. A paper published by Kurvinen et al. outlines a prototype of a UAV with detectors for mapping radioactive fallout as well as isotope identification for certain sources.¹² However, only preliminary calculations were performed on a very limited number of sources, and its impact on nuclear weapons forensics is not mentioned.

1.3.2 Post-Detonation Forensics

There is a considerable lack of open-source literature on the subject of isotopic composition of the fallout immediately following a nuclear detonation. Much of the literature regarding post-detonation isotopics involves the analysis of samples decades after the detonation, such as the analysis of samples resulting from fallout from the Trinity test on July 16, 1945.¹³ This analysis was carried out by Fahey et al. over half of

a century later in 2010. While forensic analysis at this point can still yield data of the initial weapon composition, it is not useful from the perspective of this project since rapid attribution is key to a prompt response. The forensic methodologies employed by Fahey et al. are not useful since the radiation levels will be immensely high 24 hours following detonation. Furthermore, methods used include X-ray fluorescence, light microscopy, and scanning electron microscope analyses.¹³ None of these analytical methods will be of use in the hazardous high-radiation field of a post-detonation environment.

Kraus and Foster of Sandia and Lawrence Livermore National Laboratories, respectively, have published the top dose-producing radionuclides following a uranium-fueled nuclear detonation at various time intervals after detonation.¹⁴ The purpose of this paper was to provide time-dependent lists for radiological health physics assessments. The analysis was performed utilizing the yield of a 10-kiloton highly-enriched uranium (HEU) weapon established in the National Planning Scenarios by the Department of Homeland Security.¹⁵ The authors utilize the Livermore Weapons Activation Code (LWAC) to develop a source term inventory following a uranium-fueled nuclear detonation. The analysis also utilizes the Lagrangian Operational Dispersion Integrator (LODI) model to model the dispersion of the fallout.¹⁴ Kraus and Foster acknowledge that variations in the separation mechanisms of different fallout material elements may cause significant differences in the ground-deposited radiological constituents of the soil at ground zero compared to radiological constituents of the soil at larger distances.

While it is acknowledged that these fractionation effects can prove to be significant, they are also extremely difficult to model and were therefore neglected.¹⁴

While the paper by Kraus and Foster outlines top dose-producing radiological nuclides following a uranium detonation, it does not display a gamma-ray spectrum which is necessary for the desired analysis for comparison to that of a plutonium weapon. While the nuclides are outlined, each nuclide may have hundreds of X-rays and gamma rays which contribute to the photon spectrum which will be obtained (though not necessarily all seen) on an HPGe detector. In addition, these nuclides were given for an HEU weapon with an initial enrichment of 94%. This paper also does not include analysis of nuclides and photons produced following the detonation of weapons fueled by different types of nuclear material than 94% enriched HEU, such as weapons with lower enrichments of HEU or plutonium weapons. Therefore, the analysis by Kraus and Foster begs further investigation.

2. SIMULATIONS

This chapter begins by describing how the detonation of each of the nuclear weapons was simulated. The goal of modeling these detonations was to obtain the isotopics of the fallout from each of the weapons so that the resulting photon source could be obtained. The chapter continues to then describe how the source term was obtained from the isotopics. A description of the modeled detection system is then provided, as well as the details of how the transport calculations were performed to obtain the resulting fallout spectra. The goal of this was to generate spectra which can be further analyzed with Genie for differentiation.

2.1 Modeling a Nuclear Detonation in MCNP6

The nuclear material of each weapon was modeled as a bare sphere in the Monte Carlo N-Particle Transport Code Version 6.1 (MCNP6).⁴ While a reflector may impact the energy spectra of the neutron flux and therefore the resulting isotopic composition after irradiation, the impact of the reflector is beyond the scope of this project and was therefore neglected. MCNP6 was utilized to simulate a weapons explosion by burning the nuclear material utilized in each weapon to an explosive yield of 10 kilotons of TNT. A yield of 10 kilotons was selected since this is the yield of the nuclear detonation event utilized for the National Planning Scenarios established by the Department of Homeland Security.¹⁵ This burn resulted in a list of nuclides and their respective concentrations resulting from fissions and other nuclear reactions which occurred during the burn of the material. MCNP6 tracks fission products based on which tier the user defines in the

input. In this problem, tier 3 fission products were included. These fission products are listed in Table 12 in Appendix A.

The three uranium weapons simulated contained atomic enrichments of 20%, 50% and 90% ^{235}U , with the remainder being simulated as the isotope ^{238}U . While in reality small amounts of other uranium isotopes such as ^{234}U may be present, the impact and concentrations of these isotopes are negligible and can be ignored for the purposes of this project.¹⁶ Weapons-grade plutonium was considered to be plutonium with less than or equal to 7% ^{240}Pu .¹⁷ Fuel-grade plutonium contains more than 7% but less than 19% of ^{240}Pu , while reactor-grade plutonium contains 19% or more of ^{240}Pu .¹⁷ Plutonium from most light-water and heavy-water power reactors typically has a constitution of approximately 50-65% of ^{239}Pu with the remainder mostly ^{240}Pu , ^{241}Pu , and ^{242}Pu . Table 1 displays the composition of the plutonium weapons investigated in this project. The reactor-grade plutonium was obtained from the typical isotopic composition following a burnup of 33.0 GWd/t in a pressurized water reactor (PWR).¹⁷

Table 1. Isotopics of the plutonium weapons to be investigated in this project.

Isotope	^{238}Pu	^{239}Pu	^{240}Pu	^{241}Pu	^{242}Pu
Reactor-Grade (PWR, 33.0 GWd/t)	1.7%	56.0%	24.1%	11.3%	5.4%
Weapons-Grade	~0%	95.0%	4.5%	0.4%	0.1%

The mass densities of the uranium and plutonium metal used were 18.9 g cm^{-3} and 19.6 g cm^{-3} , respectively, as given in Lamarsh.¹⁸ Burnup (BU) of nuclear material was found via

$$BU = \frac{E}{\text{Mass of Heavy Metal}}, \quad (1)$$

where E is the released energy. To maintain a constant burnup, the mass of nuclear material in both the uranium and plutonium spheres was made equivalent. To accomplish this, the radius of the plutonium sphere was made slightly less than that of the uranium sphere due to the higher density of plutonium. A radius of 25.00 cm was chosen for the uranium spheres since this maintained a neutron multiplication factor of close to at least 1.2 for each of the three enrichments. To maintain a constant mass of nuclear material for constant burnup, the radius of each of the plutonium spheres was changed to 24.67 cm. This resulted in an average burnup of 0.391 megawatt days per kilogram of heavy metal.

The MCNP6 card ‘kcode’ was utilized in a burn run with an initial criticality guess of 1.0. This utilized 5000 particles per cycle with 100 cycles total, however skipping the first 10 cycles to allow for source convergence. The explosion was simulated by burning the sphere for 10.0 ms in three equal 3.33 ms intervals at full power of the explosion, followed by a fourth time step with a simulated power of 0 for 24 hours to allow for decay. Due to the limited information in the literature of the weapon detonation time, 10.0 ms was assumed as a reasonable value for the purposes of this analysis since no significant decay or transmutation will be occurring on this time scale which will impact results. The power in MCNP6 is input in MW.⁵ System power (P) is assumed to be constant throughout the detonation for the purposes of this project, and can therefore be calculated from

$$P = \frac{E}{t}, \quad (2)$$

where t defines the time over which the energy E was released. A single ton of TNT converts to $4.184 \cdot 10^9$ J, which means that 10 kilotons of TNT releases $4.184 \cdot 10^{13}$ J. Using Eq. (2), this amount of energy released over 10.0 ms results in a power of $4.184 \cdot 10^9$ MW. Cross sections for neutrons were obtained at 293.6 K from the .80c neutron libraries in the Evaluated Nuclear Data Files ENDF/B-VII.

The values for system criticality are provided in Figure 6 for the 8 burnup steps. Error bars are present but are difficult to see. All of the values are above unity and therefore denote supercritical systems. For the purposes of these simulations, it is desired that each of the systems be supercritical since a nuclear bomb would be as well.

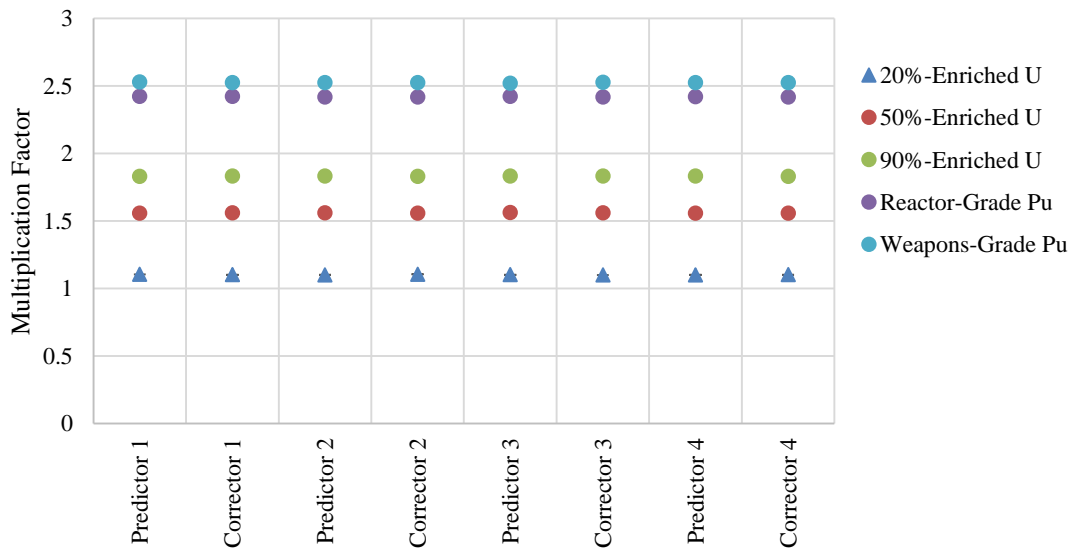


Figure 6. Multiplication factors for each weapon for each burnup step.

In order to verify the assumption that a 10.0 ms detonation time was accurate for the purposes of this project, the burn time was decreased by a factor of 1000 to 10.0 μ s. To hold the burnup and yield constant, the power was increased by a factor of 1000 to $4.184 \cdot 10^{12}$ MW. This was performed for the 90% enriched uranium weapon. Results displayed that the maximum difference in any of the nuclide number density concentrations at the end of the run was 0.06%, a negligible difference. Furthermore, it was desired to ensure that a sufficient number of burn steps were being utilized to allow for convergence. Therefore, the number of burn steps was increased from three to five with a corresponding decrease in each of the burn time intervals to maintain a constant burnup. The resulting maximum difference in any of the number density concentrations was 0.35%, also a negligible difference. These results display that the burnup time and the number of burnup steps being utilized were sufficient. An example MCNP6 input deck for the burnup run on a 20%-enriched uranium sphere is given in Appendix D.

The distribution of the fissioning isotopes was analyzed and the results are displayed in Table 2 for the first of three corrector steps. The predictor steps are not displayed here. This variation in the distribution of fissioning isotopes should lead to a variation in gamma-emitting fission products which can be resolved on an HPGe detector. For example, as the enrichment of uranium increases, the amount of fissions in ^{238}U decreases significantly. For the 20%-enriched uranium weapon, the amount of ^{238}U fissioning is almost 23%, compared to just over 1% for the 90%-enriched uranium weapon. Table 3 displays the average neutron energy causing fission for each of the

weapon loadings. Only the last corrector step is shown for each weapon loading since the value fluctuated by less than 1%.

Table 2. Number of fissions per second for various isotopes in each weapon for the first corrector step.

Nuclide	20%- Enriched U	50%- Enriched U	90%- Enriched U	Reactor- Grade Pu	Weapons- Grade Pu
²³⁵ U	$1.06 \cdot 10^{26}$	$1.20 \cdot 10^{26}$	$1.28 \cdot 10^{26}$	$1.77 \cdot 10^{14}$	$1.72 \cdot 10^{14}$
²³⁸ U	$2.38 \cdot 10^{25}$	$1.04 \cdot 10^{25}$	$1.75 \cdot 10^{24}$	$4.15 \cdot 10^{13}$	$1.27 \cdot 10^{12}$
²³⁶ Pu	~0	~0	~0	0	0
²³⁷ Pu	~0	~0	~0	$6.93 \cdot 10^{17}$	$4.68 \cdot 10^{16}$
²³⁸ Pu	~0	~0	~0	$2.43 \cdot 10^{24}$	$1.50 \cdot 10^{19}$
²³⁹ Pu	~0	~0	~0	$8.19 \cdot 10^{25}$	$1.20 \cdot 10^{26}$
²⁴⁰ Pu	~0	~0	~0	$2.05 \cdot 10^{25}$	$3.50 \cdot 10^{24}$
²⁴¹ Pu	~0	~0	~0	$1.60 \cdot 10^{25}$	$4.83 \cdot 10^{23}$
²⁴² Pu	~0	~0	~0	$3.72 \cdot 10^{24}$	$6.34 \cdot 10^{22}$
²⁴³ Pu	0	0	0	$1.99 \cdot 10^{19}$	$2.68 \cdot 10^{17}$
²⁴⁴ Pu	0	0	0	~0	~0

Table 3. Average neutron energy causing fission.

Weapon Loading	Last Corrector Step Energy (MeV)
20%-Enriched U	1.13
50%-Enriched U	1.11
90%-Enriched U	1.21
Reactor-Grade Pu	1.61
Weapons-Grade Pu	1.63

2.2 Modeling a Post-Detonation Environment with an HPGe Detector

The photon emission distribution based on the isotopics, their atom fractions, and photon yield data was found using data from the National Nuclear Data Center.¹⁹ This photon source distribution was input into an MCNP6 input file with the HPGe detector

modeled. The HPGe detector modeled was the Low Energy Germanium Detector (LEGe) by Canberra. The model number was GL0515R-DET and the serial number was 8828. The crystal was modeled in MCNP6 with the characteristics given in Table 4. A side-view of the crystal is shown in Figure 7. The dimensions and parameters for the detector were obtained in several personal communications with CANBERRA.^{20,21} The electronics, casing, and endcap of the detector were not modeled since the materials and geometry for these features could not be obtained from CANBERRA or via a literature review. The assumption to neglect these features should not significantly impact results. These features will simply introduce slightly more scattering which can be subtracted out when Genie is utilized to analyze results.

Table 4. Germanium crystal and window properties for the GL0515R HPGe detector.

Parameter	Value
Crystal Diameter (mm)	25.00
Crystal Length/Thickness (mm)	15.30
Groove Inner Diameter (mm)	8.0
Groove Outer Diameter (mm)	13.0
Front Dead Layer (mm)	$0.3 \cdot 10^{-3}$
Side Dead Layer (mm)	0.5
Back Dead Layer (mm)	0.5
Window Material	Aluminum
Window Thickness (mm)	0.500
Distance from Window (mm)	5.00

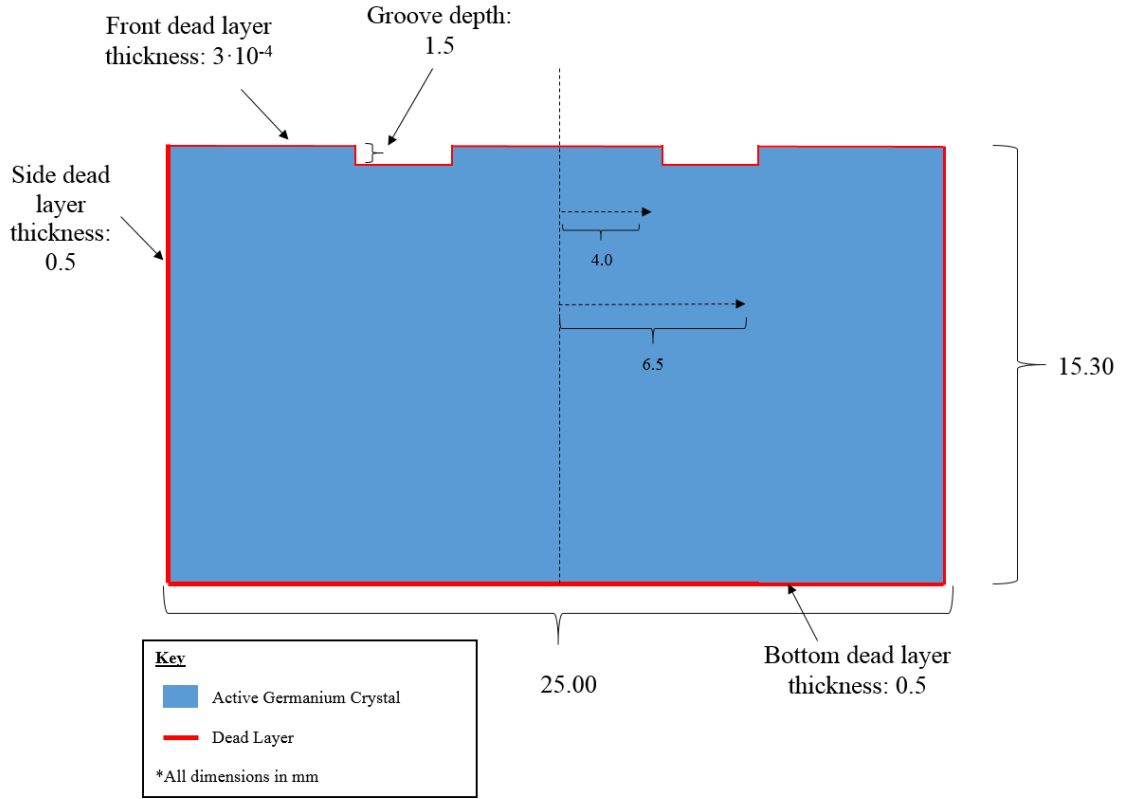


Figure 7. Side-view of the germanium crystal for the GL0515R HPGe detector with dimensions in units of mm.

When modeling a detector in MCNP6, it is necessary to input values for Gaussian Energy Broadening (GEB). This allows the code to approximately model the statistical, non-linear Gaussian broadening nature of the photopeaks with the resolution of the detector. Full Width at Half Maximum (FWHM) can be approximated by

$$FWHM = a + b\sqrt{E + cE^2}, \quad (3)$$

where $FWHM$ is in units of MeV; E is the energy of the photon in MeV; and a , b , and c are the GEB parameters for the detector in units of MeV, $\text{MeV}^{1/2}$, and MeV^{-1} , respectively. The GEB parameters can be found experimentally.⁵ Since there are three

unknowns, three FWHM values at three separate energies are needed. These measurements were not possible with the GL0515R detector due to departmental circumstances, and therefore these parameters were obtained from a similar detector, the GeMini (MINIature Germanium spectrometer), a mechanically-cooled HPGe detection system with a crystal 50 mm in length and 47 mm in diameter.²² While the resolution of an HPGe crystal may vary slightly amongst various conditions and detectors, it is believed that for the purposes of this work the GEB parameter will not be of a large impact as long as it remains consistent with the use of a germanium crystal. Table 5 displays the values utilized to calculate the constants a , b , and c . This resulted in values for the constants a , b , and c of 0.002794 MeV, $4.123 \cdot 10^{-4} \text{ MeV}^{1/2}$, and 1.402 MeV^{-1} , respectively.

Table 5. Values utilized to find the GEB parameters.

Energy (keV)	FWHM (keV)
122	2.95
662	3.26
1332	3.60

A soil sample with a radius of 3 cm was modeled and placed with its bottom located at 1.45 cm above the top face of the aluminum window, as shown in Figure 8. The setup includes the HPGe detector suspended in the center of the problem within air. The ground was modeled as soil 30 cm below the bottom of the HPGe detector. The problem boundary was modeled as a sphere with a radius of 500 cm. The face of the

detector is pointing upwards in the positive z direction. The setup is displayed in Figure

9. This figure was plotted in Xming, an open-source MCNP geometry plotter.²³

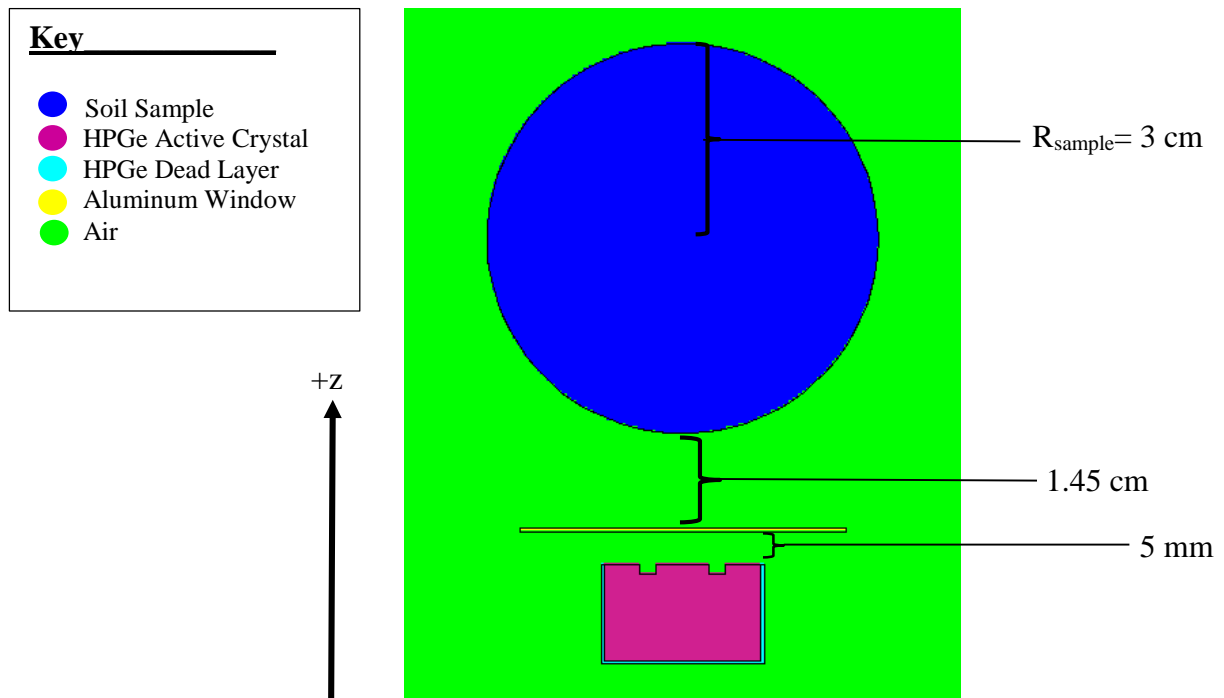


Figure 8. MCNP6 model of germanium crystal, aluminum window, and soil sample plotted in Xming.

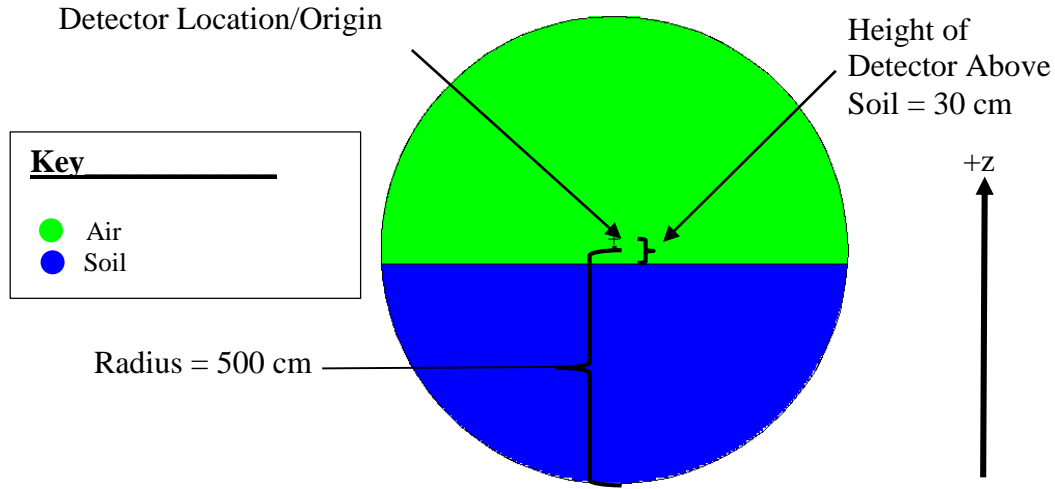


Figure 9. Overall problem geometry in MCNP6 plotted in Xming.

The source was biased downwards towards the direction of the face of the HPGe detector using a SBn source biasing tally with an exponential sampling bias given by

$$p(\mu) = e^{a|\mu|}, \quad (4)$$

where μ is a random variable, and a is a parameter of the built-in function which determines the amount of biasing to be implemented.⁵ The larger the value of a , the more biasing occurs, and the weight of the particle is adjusted appropriately in order to maintain the integrity of the problem. A value of 5 was chosen for a and was deemed sufficient for this analysis. To sample uniformly inside of a spherical volume source, the sampling distribution is proportional to the square of the radius, since this represents a differential volume element, as shown by

$$\frac{dV}{dr} = \frac{d\left(\frac{4}{3}\pi r^3\right)}{dr} = 4\pi r^2, \quad (5)$$

where r and V represent the radius and volume of the sphere, respectively. Therefore, in order to sample uniformly from a spherical volume source in MCNP, the card “SPn -21 2” must be used.⁵

An F8 pulse height tally was utilized on the active region of the HPGe detector with 1000 equally-spaced energy bins of 2 keV in width ranging from 0 MeV to 2 MeV. This tally gives the energy distribution of pulses created in a detector by radiation.⁵ A value of 1E8 initial starting photons was shown to result sufficient counting statistics for the purposes of this analysis.

In order to model the photon radioactivity coming from the soil, in a separate file the photon source was modeled at the soil surface as a plane source with an area of 1 m² and the results were added to those from the soil sample run. The same number of initial starting particles were ran and the same source biasing was used to bias particles in the direction of the detector. The error was propagated according to the error propagation formula given by

$$\sigma_U^2 = \left(\frac{\partial U}{\partial x}\right)^2 \cdot \sigma_x^2 + \left(\frac{\partial U}{\partial y}\right)^2 \cdot \sigma_y^2 + \dots, \quad (6)$$

where x and y are the two values which a function is being performed upon and U is the desired result.¹

Air and soil were modeled according to the Compendium of Material Composition Data for Radiation Transport Modeling given by Pacific Northwest

National Laboratory.²⁴ Compositions for dry air near sea level and soil (earth, U.S. average) are given in Table 6 and Table 7, respectively. The densities of the air and soil used were 0.001205 g cm⁻³ and 1.52 g cm⁻³, respectively.²⁴ Cross sections for photons were obtained from the .84p cross section library from ENDF/B-VII.

Table 6. Composition of air to be used in MCNP.

Element	Photon ZA	Weight Fraction	Atom Fraction
C	6000	0.000124	0.000150
N	7000	0.755268	0.784431
O	8000	0.231781	0.210748
Ar	18000	0.012827	0.004671

Table 7. Composition of soil to be used in MCNP.

Element	Photon ZA	Weight Fraction	Atom Fraction
O	8000	0.513713	0.670604
Na	11000	0.006140	0.005578
Mg	12000	0.013303	0.011432
Al	13000	0.068563	0.053073
Si	14000	0.271183	0.201665
K	19000	0.014327	0.007653
Ca	20000	0.051167	0.026664
Ti	22000	0.004605	0.002009
Mn	25000	0.000716	0.000272
Fe	26000	0.056283	0.021050

In a real-life detonation scenario, neutron activation in the ground or surrounding buildings may cause additional photon activity; however this was ignored for the purposes of this analysis. Furthermore, it was assumed that the nuclear material is dispersed uniformly and any variations of isotopics in the fallout distribution was

neglected for the purposes of this simulation. As mentioned in Kraus and Foster, fractionation effects due to the different physical separation mechanisms of the various radionuclides may cause a different radionuclide mixture near ground zero compared to mixtures at greater distances.¹⁴ Kraus and Foster also acknowledge that while these effects may be significant, they are extraordinarily difficult to predict.¹⁴ Therefore, these effects were not included.

An example MCNP6 input deck for the 20%-enriched uranium fallout source with the detector is given in Appendix E. In this input deck, the photon source is modeled as originating from the soil sample and not from the ground. The input deck with the ground source, or additional input decks, may be obtained upon written request. Furthermore, the fallout photon source from additional types of initial fissile material may be obtained upon request.

The photon spectra resulting from a gamma analysis of the fallout from the 20%-enriched uranium weapon is shown in Figure 10. Numerous photopeaks can be resolved, including a peak at 108 keV due to decay of ^{239}Np , a peak at 232 keV due to decay of ^{132}Te , a peak at 250 keV due to decay of ^{135}Xe , a peak at 278 keV due to decay of ^{239}Np , and a peak at 293 keV due to decay of ^{143}Ce . It should be noted that these peaks are only accurate to within 2 keV, since this was the bin width used in MCNP6 to obtain reasonable counting statistics. For instance, the true energy of the gamma emitted from the decay of ^{239}Np is 106.123 keV, but falls within the 106 to 108 keV energy bin.¹⁶ It should be noted that actual detectors typically utilize more energy bins than were used for this project; however, the bins widths and number of bins utilized for this analysis

were chosen in order to obtain reasonable counting statistics. It is not expected that this modeling assumption will impact results.

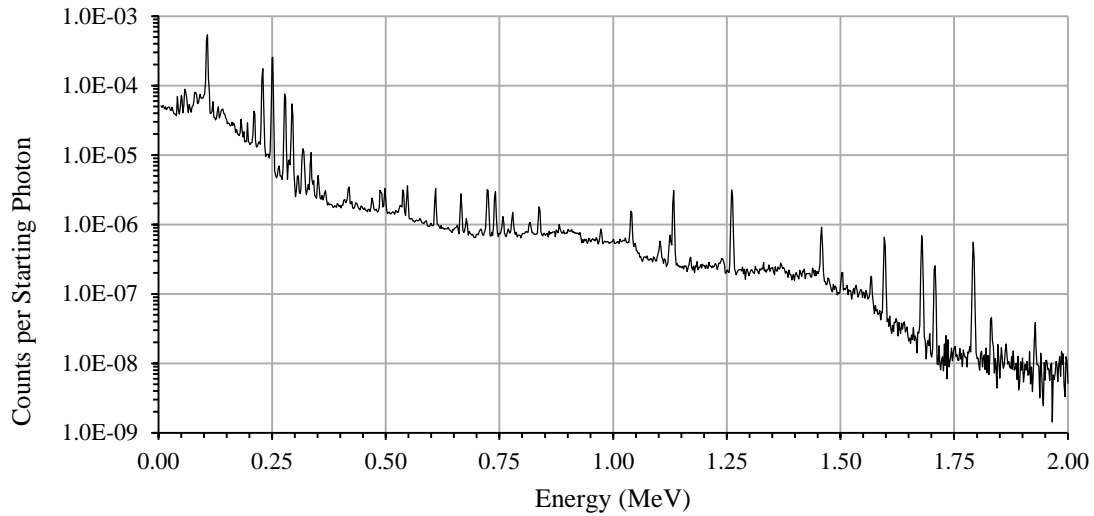


Figure 10. Photon spectrum on an HPGe detector simulated in MCNP6 24 hours after the detonation of a 10-kiloton weapon fueled with 20%-enriched uranium.

Figure 11 shows the photon spectrum obtained from the detonation of a 50%-enriched uranium weapon. It is evident that the peak at 108 keV has decreased considerably compared to that of the 20% spectrum, and the peak at 250 keV is much larger. The peak at 278 keV has also decreased considerably.

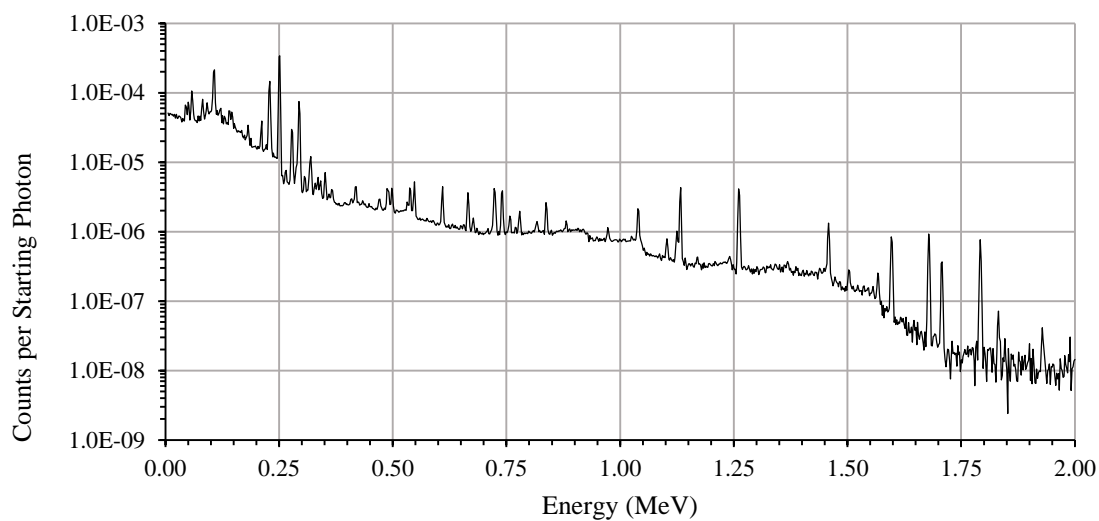


Figure 11. Photon spectrum on an HPGe detector simulated in MCNP6 24 hours after the detonation of a 10-kiloton weapon fueled with 50%-enriched uranium.

Figure 12 shows the photon spectrum obtained from the detonation of a 90%-enriched uranium weapon. The peak at 108 keV has decreased even more from the 50%-enriched uranium spectrum, and the peak at 250 keV is slightly larger. The peak at 278 keV is no longer evident.

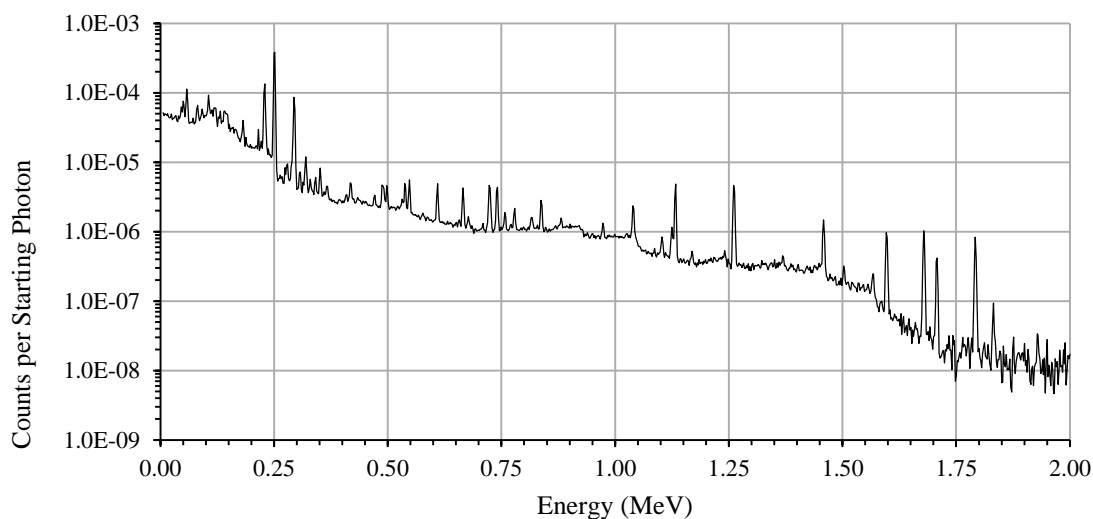


Figure 12. Photon spectrum on an HPGe detector simulated in MCNP6 24 hours after the detonation of a 10-kiloton weapon fueled with 90%-enriched uranium.

The photon spectra obtained from the detonation of reactor-grade and weapons-grade plutonium weapons are given in Figure 13 and Figure 14, respectively. These two spectra have a large resemblance to that of the 90%-enriched uranium, with the exception of an additional peak in the plutonium spectra at 319 keV due to the full energy deposition of the gamma ray emission from the decay of ^{105}Rh . Unfortunately, the two plutonium spectra seem close to identical to each other based on an initial analysis. Further analysis with Genie may be able to identify differentiating factors between the two. The relative errors for the 20%-enriched uranium, 50%-enriched uranium, 90%-enriched uranium, reactor-grade plutonium, and weapons-grade plutonium fallout spectra are displayed in Appendix B in Figure 39, Figure 40, Figure 41, Figure 42, and Figure 43, respectively.

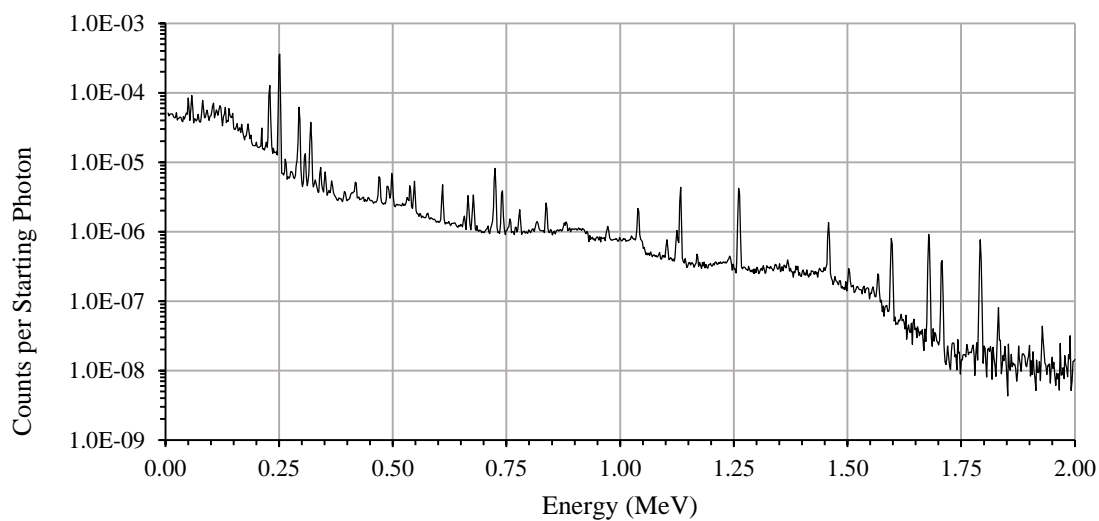


Figure 13. Photon spectrum on an HPGe detector simulated in MCNP6 24 hours after the detonation of a 10-kiloton weapon fueled with reactor-grade plutonium.

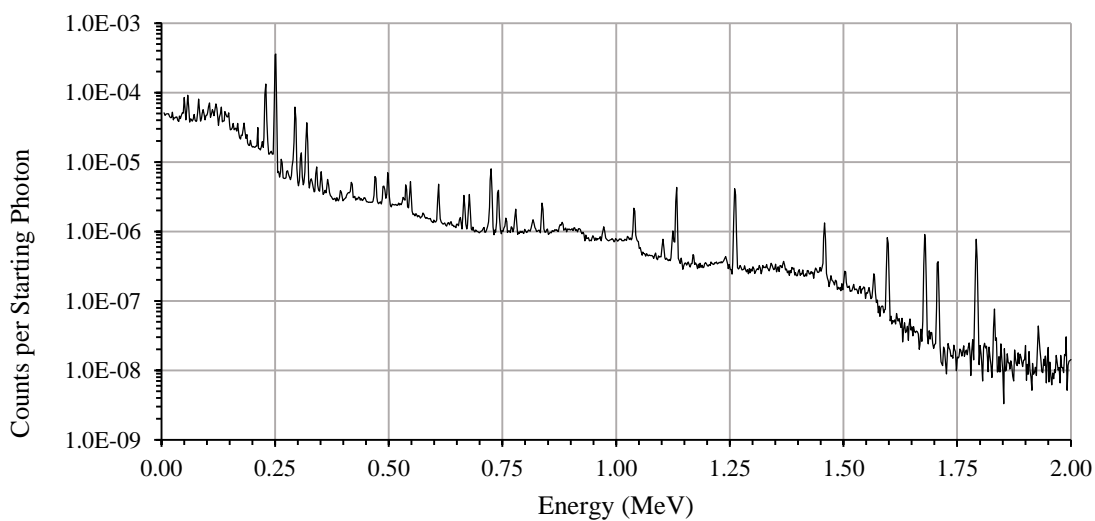


Figure 14. Photon spectrum on an HPGe detector simulated in MCNP6 24 hours after the detonation of a 10-kiloton weapon fueled with weapons-grade plutonium.

3. ANALYSIS IN GENIE

This chapter describes the use of Genie basic spectroscopy software to analyze the spectra generated. Genie is used to identify peaks present for four energy groups and subtract out what it identifies to be background and scattering from higher-energy peaks. When peaks are significantly different between fallout spectra, ratios are generated in order to quantify these differences. These ratios are used to differentiate between several types of initial nuclear weapons loadings. Additional spectral features, or the lack thereof, are then discussed. The next section discusses the causes of the inability to differentiate between fallout spectra from reactor-grade and weapons-grade plutonium. Finally, an algorithm to identify the initial weapon loading based on ratios of peaks from these fallout spectra is provided.

3.1 VMS Standard Peak Search

Genie has multiple types of peak search algorithms which can be implemented. One of these algorithms is the VMS Standard Peak Search. According to the Genie 2000 manual, this method locates all peaks within the channel search interval above a sensitivity threshold using a second differential peak location method, and fits them with a pure Gaussian fit routine.²⁵ It is suited for a case where the contents of the spectrum are unknown. Since this would likely be the case in a nuclear detonation, this method was deemed acceptable for this project. This search was performed through the entire range of channels from 1 to 1024. The peak search sensitivity defines the number of standard deviations above background a feature on the spectrum must be to be identified

as a peak.²⁵ The Gaussian sensitivity describes how close the shape of the peak should match to that of a pure Gaussian. Lower settings within the 5-10 range force the algorithm to identify peaks more closely shaped as a Gaussian.²⁵ Both of these settings were manipulated and the settings of 3.00 and 10.00 for the peak search and Gaussian sensitivity, respectively, were deemed acceptable for this analysis. Once the peaks were identified, the list of peaks were split into four energy groups and plotted for a more in-depth analysis. An arbitrary counting time of $4.9999 \cdot 10^4$ s was input into Genie to calculate count rates, and resulting values are based on this live counting time. This counting time is arbitrary since no time was provided to MCNP6 for the photon transport calculation. The results of the spectra were provided in units of counts per starting photon. This was then multiplied by $1 \cdot 10^{10}$ so that it could be analyzed in Genie, since Genie needs whole numbers to operate properly. In order to reach this number of starting particles, a calculation was done with the activities resulting from the burnup runs. The maximum of all of the five required resulting counting times was 219 s. A count of this length is very reasonable in the field.

3.2 Energy Group 1

The identified peaks up to approximately 320 keV for the 20%-enriched, 50%-enriched, and 90%-enriched uranium weapons are given in Figure 15, Figure 16, and Figure 17, respectively. Error bars are present but are extremely small and therefore difficult to visualize.

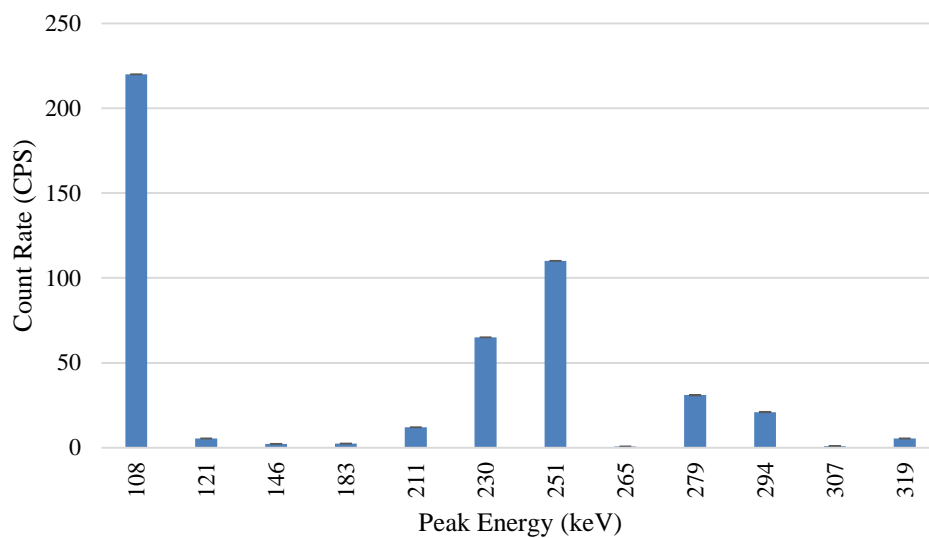


Figure 15. Peaks identified in Genie for the first analyzed energy group of the 20%-enriched uranium fallout spectrum.

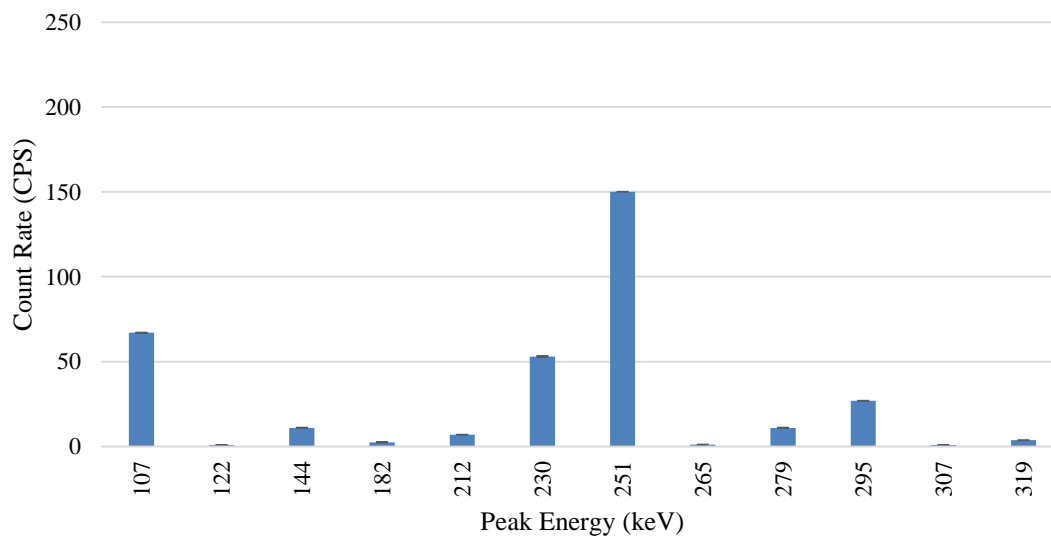


Figure 16. Peaks identified in Genie for the first analyzed energy group of the 50%-enriched uranium fallout spectrum.

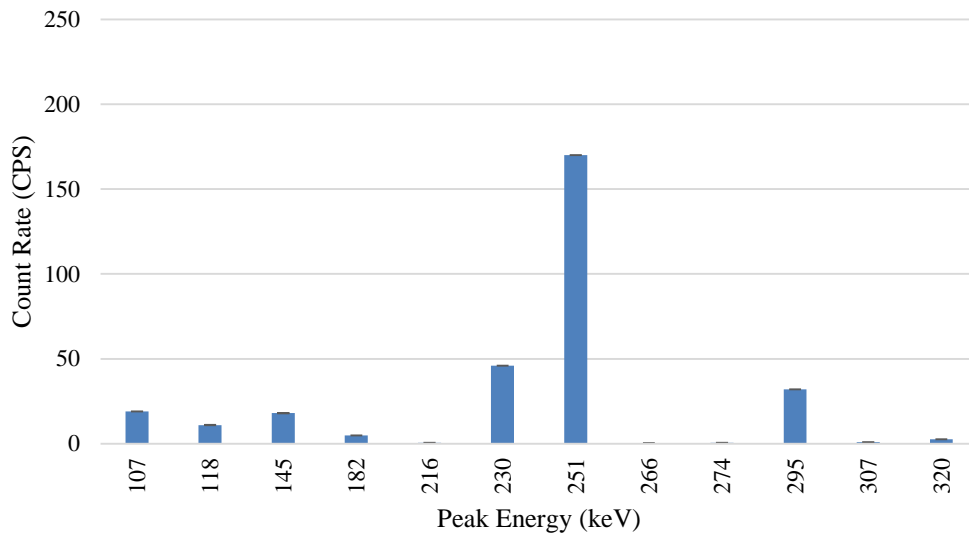


Figure 17. Peaks identified in Genie for the first analyzed energy group of the 90%-enriched uranium fallout spectrum.

In all of the uranium fallout spectra, it can clearly be seen how the height of the 108 keV peak due to the full energy deposition of the photon from beta decay of ^{239}Np decreases drastically as the enrichment of the initial weapon increases. As mentioned before, the true energy of this peak is 106.123 keV, but is tallied within the 106 keV to 108 keV bin by MCNP.¹⁶ This decreasing peak height makes sense, since ^{239}Np ($t_{1/2} = 2.3565$ days) is a decay product of ^{239}U ($t_{1/2} = 23.45$ minutes) which is produced by neutron capture in ^{238}U .¹⁶ As ^{238}U concentration increases in the initial loading, more neutron capture will occur in this nuclide and therefore more ^{239}Np will be produced. For the purposes of this analysis, an insignificant amount of decay of ^{239}Np to ^{239}Pu occurs since the half-life is over 2 days and the spectra provided in this investigation are given at 24 hours post-detonation.

Once the initial weapon can be identified to be of uranium composition, analysis of the 108 keV peak can provide a simple and effective technique to be able to make a rough estimate of the initial enrichment. To make the comparison of the spectra independent of the number of counts, ratios of the peak at 108 keV and the peak at 251 keV due to ^{135}Xe can be obtained. These ratios are displayed in Table 8. Uncertainties are included but are so small that most of the values round to zero. This can give a rough estimate for the initial enrichment. Future analysis could focus on the identification of this gamma ratio at additional enrichments for a more precise estimate. Note that the 108 keV peak was not identified on either of the plutonium spectra. Therefore, identification of this peak may be an effective method of differentiating the fallout from a uranium and plutonium weapon. The enrichment of the initial uranium weapon versus the ratio of these two peaks was plotted and is given in Figure 18. Error bars are present but are too small to see. A best-fit equation was chosen which gave an R^2 value closest to 1 while preserving a physical result.

Table 8. Analysis of 108 keV and 251 keV peaks to determine initial uranium enrichment in the weapon.

Weapon Loading	108 keV Counts per Second	251 keV Counts per Second	Ratio
20%-Enriched U	$220.00 \pm 0.0\%$	$110.00 \pm 0.0\%$	$2.0000 \pm 0.0\%$
50%-Enriched U	$67.00 \pm 0.1\%$	$150.00 \pm 0.0\%$	$0.4467 \pm 0.1\%$
90%-Enriched U	$19.00 \pm 0.3\%$	$170.00 \pm 0.0\%$	$0.1118 \pm 0.3\%$
Reactor-Grade Pu	Not Present	$160.00 \pm 0.0\%$	~ 0
Weapons-Grade Pu	Not Present	$160.00 \pm 0.0\%$	~ 0

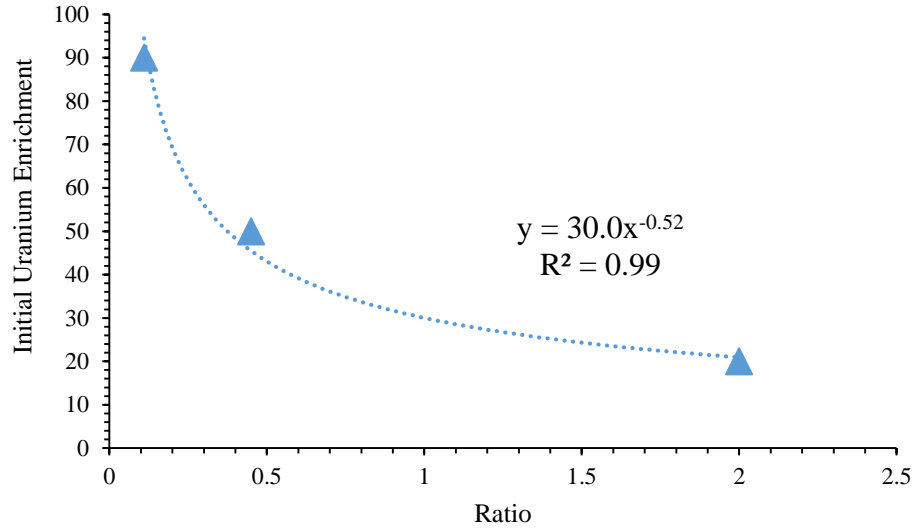


Figure 18. Initial uranium enrichment versus the ratio of the 108 keV to the 251 keV peak count rates.

The peaks identified in the plutonium spectra up to 320 keV are shown in Figure 19 and Figure 20 for reactor-grade and weapons-grade plutonium fallout spectra, respectively. The two plutonium spectra show a large resemblance to that of the 90%-enriched uranium spectrum, with the exception of a larger count value for the peak at 320 keV due to ^{105}Rh . As mentioned before for ^{239}Np , the true height of the peak for ^{105}Rh is 318.9 keV, however this is tallied in the 320 keV bin due to the 2 keV bin width in the MCNP6 input file.¹⁶ For 1 MeV neutron fissions of ^{239}Pu , ^{105}Rh has a direct fission yield of $3.652 \cdot 10^{-7}$ atoms per fission and an accumulated yield of $5.391 \cdot 10^{-2}$ atoms per fission.¹⁶ For the same energy neutrons in ^{238}U and ^{235}U , ^{105}Rh has direct yields of $6.224 \cdot 10^{-10}$ atoms per fission and $7.560 \cdot 10^{-10}$ atoms per fission, respectively, and accumulated yields of $3.939 \cdot 10^{-2}$ atoms per fission and $1.205 \cdot 10^{-2}$ atoms per fission,

respectively.¹⁶ Since these values are significantly lower than those of ^{239}Pu , the result of a higher ^{105}Rh fission product content in the fallout for the plutonium weapons seems reasonable.

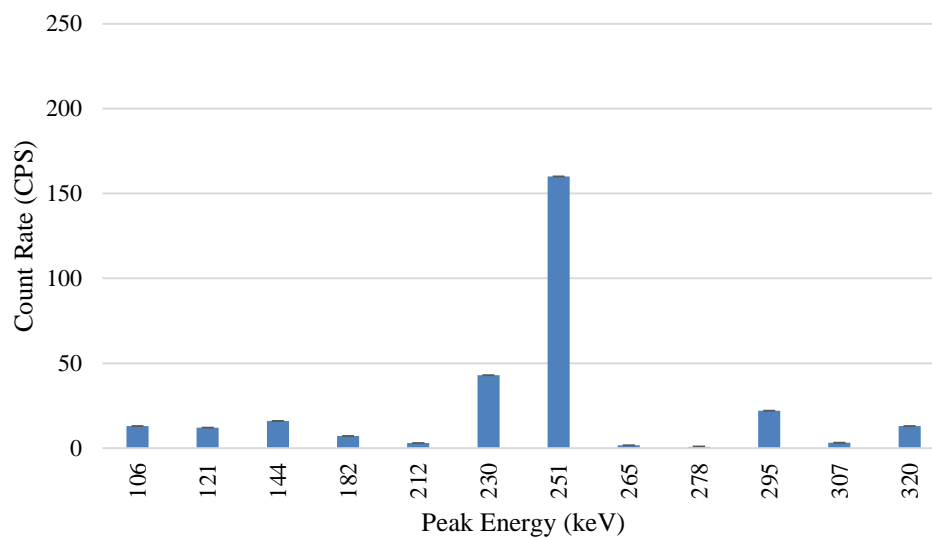


Figure 19. Peaks identified in Genie for the first analyzed energy group of the reactor-grade plutonium fallout spectrum.

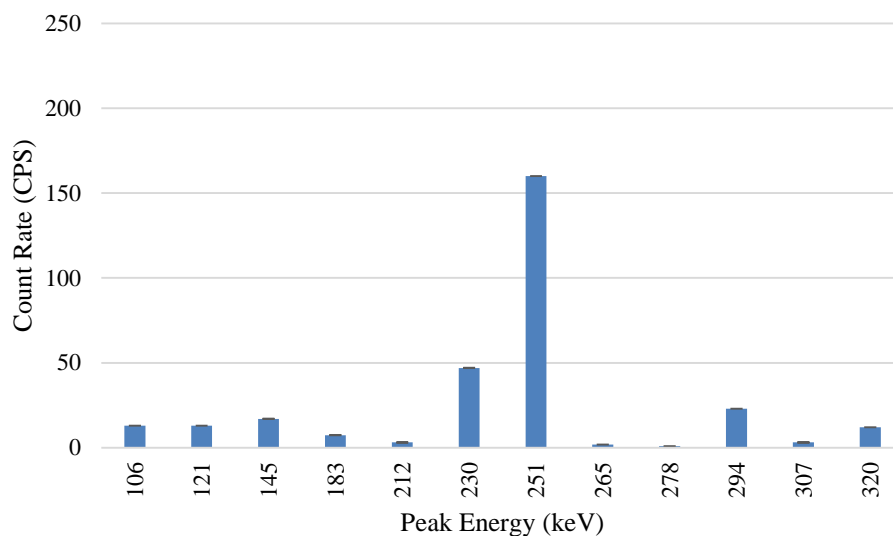


Figure 20. Peaks identified in Genie for the first analyzed energy group of the weapons-grade plutonium fallout spectrum.

In order to differentiate the plutonium spectra from the uranium spectra, the photopeak at 320 keV due to ^{105}Rh can be utilized to form ratios to the value of the peak located at 251 keV. The results are displayed in Table 9. Note that as the uranium enrichment increases, the ratio between the 320 keV and the 251 keV peak decreases substantially. Therefore, if the ratio of these two peaks can be determined to be above 0.06 the initial weapon was likely plutonium. However, if the ratio of the 320 keV and the 251 keV peaks is below this value the initial weapon was likely highly-enriched uranium. The enrichment of the initial uranium weapon versus the ratio of these two peaks is given in Figure 21. Error bars are present but are too small to see. A best-fit equation was chosen which gave an R^2 value closest to 1 while preserving a physical result.

Table 9. Analysis of 320 keV and 251 keV peaks to differentiate a uranium weapon from a plutonium weapon.

Weapon Loading	320 keV Counts per Second	251 keV Counts per Second	Ratio
20%-Enriched U	$5.40 \pm 0.4\%$	$110.00 \pm 0.0\%$	$0.0491 \pm 0.4\%$
50%-Enriched U	$3.70 \pm 0.6\%$	$150.00 \pm 0.0\%$	$0.0247 \pm 0.6\%$
90%-Enriched U	$2.70 \pm 0.7\%$	$170.00 \pm 0.0\%$	$0.0159 \pm 0.7\%$
Reactor-Grade Pu	$13.00 \pm 0.2\%$	$160.00 \pm 0.0\%$	$0.0813 \pm 0.2\%$
Weapons-Grade Pu	$12.00 \pm 0.2\%$	$160.00 \pm 0.0\%$	$0.0750 \pm 0.2\%$

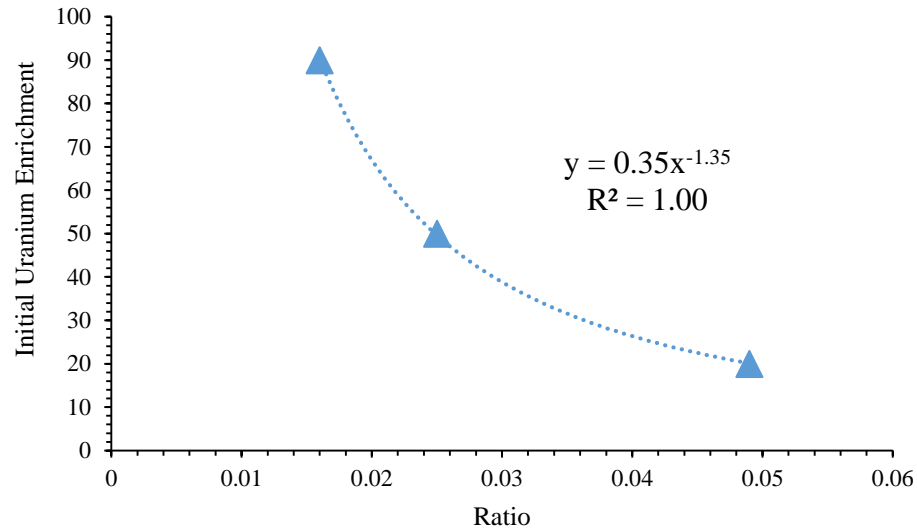


Figure 21. Initial uranium enrichment versus the ratio of the 320 keV to the 251 keV peak count rates.

3.3 Energy Group 2

The peaks in the five spectra were then separated into a second group ranging from approximately 367 keV to 837 keV. The peaks identified in the uranium spectra in this second group are displayed in Figure 22, Figure 23, and Figure 24 for the 20%-enriched, 50%-enriched, and 90%-enriched uranium weapons, respectively.

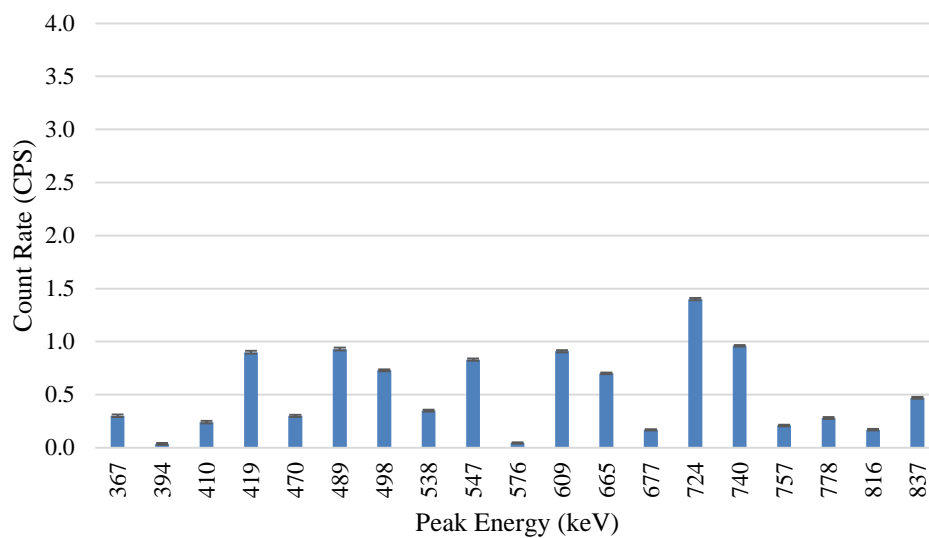


Figure 22. Peaks identified in Genie for the second analyzed energy group of the 20%-enriched uranium fallout spectrum.

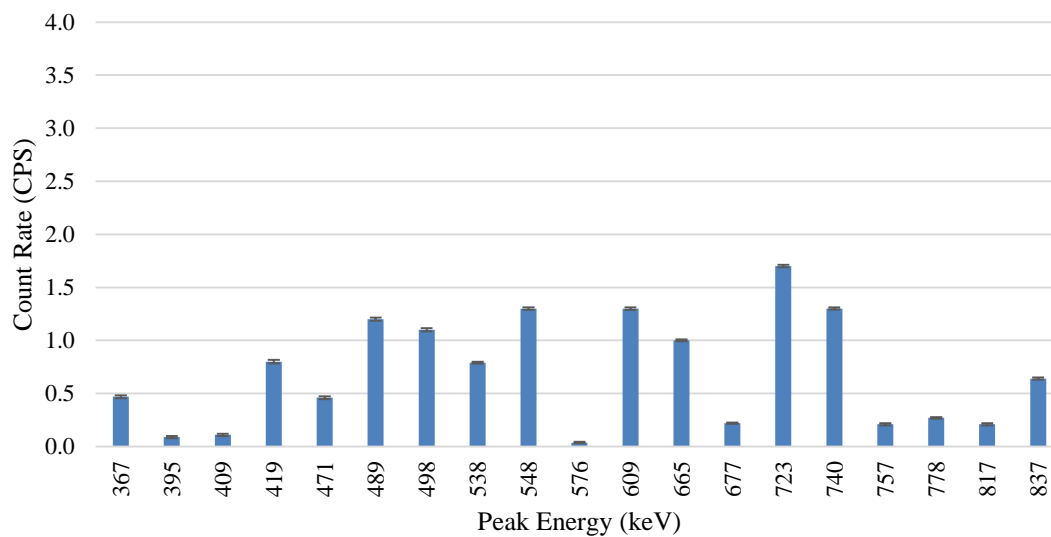


Figure 23. Peaks identified in Genie for the second analyzed energy group of the 50%-enriched uranium fallout spectrum.

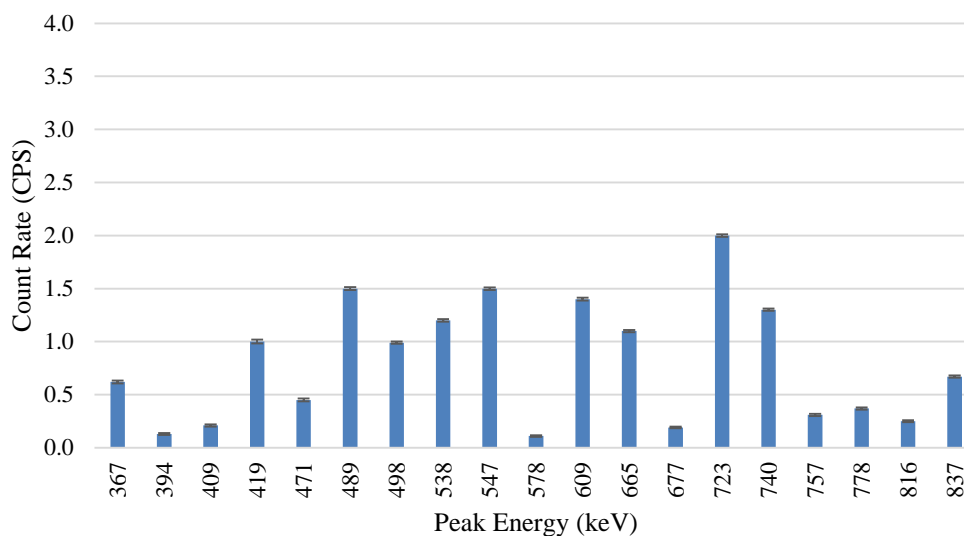


Figure 24. Peaks identified in Genie for the second analyzed energy group of the 90%-enriched uranium fallout spectrum.

The count rates for the second group of energy peaks within the spectra for reactor-grade and weapons-grade plutonium weapons are displayed in Figure 25 and Figure 26, respectively. A peak at 498 keV due to ^{103}Ru can be identified for both plutonium spectra, and it seems that the count rate for this peak is significantly higher than that of the uranium spectra. The accumulated fission yield of ^{103}Ru for ^{239}Pu fissions is almost twice that of ^{235}U for 1 MeV neutrons, and therefore behavior of this peak is as expected.¹⁶ Furthermore, upon inspection of the source definition in the MCNP6 photon transport input file, the photon source activity given to this peak at 498 keV due to ^{103}Ru is significantly higher for both of the plutonium fallout sources, which are on the order of 10^{16} photons emitted per second, than the uranium fallout sources, which are on the order of 10^{15} photons emitted per second.

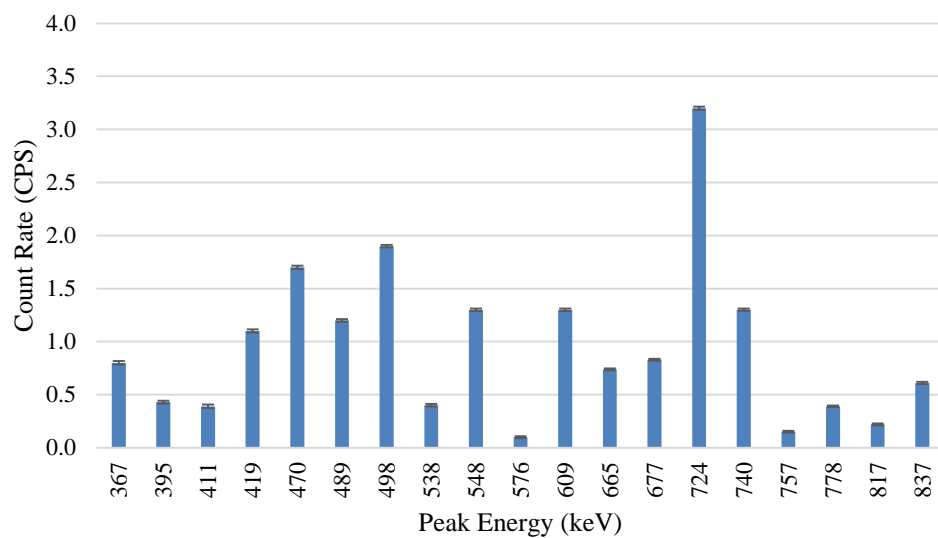


Figure 25. Peaks identified in Genie for the second analyzed energy group of the reactor-grade plutonium fallout spectrum.

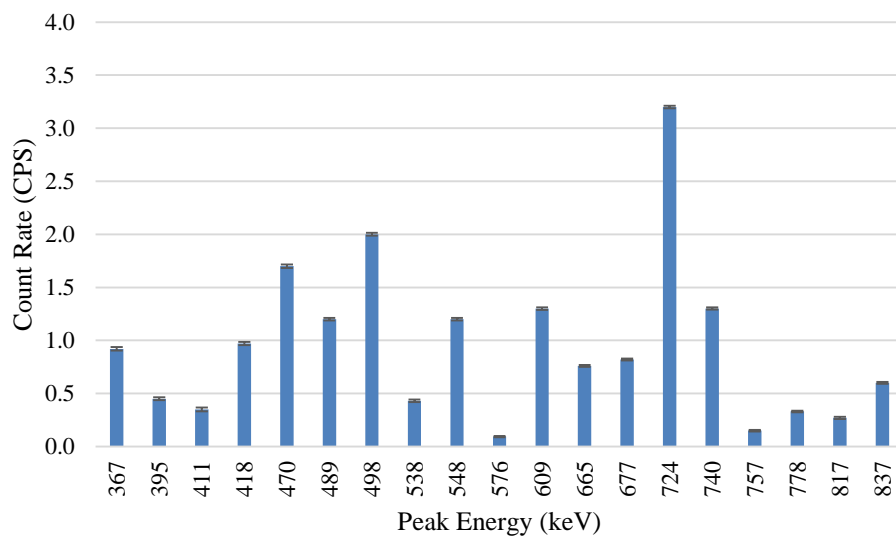


Figure 26. Peaks identified in Genie for the second analyzed energy group of the weapons-grade plutonium fallout spectrum.

If a ratio is obtained between the peak count rate value at 498 keV and that of the 837 keV photopeak due to ^{135}I , which seems to remain relatively constant between the 5 spectra, this could be an additional effective method of differentiating between uranium and plutonium fallout. A quick literature search reveals that the accumulated fission yields for ^{135}I are 0.0623, 0.0678, and 0.0605 atoms per fission for ^{235}U , ^{238}U , and ^{239}Pu , respectively.¹⁶ These values are relatively constant, and therefore the peak count rate of this nuclide's photon emission should also remain relatively constant. When consulting the source definitions in the MCNP6 input file, the activities for this photon emission are all within 9% of each other. The results of the peak comparison method are displayed in Table 10. It shows that if the ratio of these peaks is less than approximately 2, the initial weapon was likely uranium. If the ratio is greater than or equal to approximately 3, it was likely plutonium.

Table 10. Analysis of 498 keV and 837 keV peaks to differentiate between uranium and plutonium fallout.

Weapon Loading	498 keV Counts per Second	837 keV Counts per Second	Ratio
20%-Enriched U	$0.73 \pm 1.2\%$	$0.47 \pm 2.0\%$	$1.55 \pm 2.3\%$
50%-Enriched U	$1.10 \pm 1.4\%$	$0.64 \pm 1.5\%$	$1.72 \pm 2.1\%$
90%-Enriched U	$0.99 \pm 1.1\%$	$0.67 \pm 1.5\%$	$1.48 \pm 1.9\%$
Reactor-Grade Pu	$1.90 \pm 0.7\%$	$0.61 \pm 1.6\%$	$3.11 \pm 1.7\%$
Weapons-Grade Pu	$2.00 \pm 0.7\%$	$0.60 \pm 1.6\%$	$3.33 \pm 1.7\%$

3.4 Energy Group 3

The third group of peak energies analyzed in Genie ranged from approximately 879 keV to 1260 keV. The peaks in the uranium spectra in the third energy group are displayed in Figure 27, Figure 28, and Figure 29 for the 20%-enriched, 50%-enriched, and 90%-enriched uranium weapons, respectively. Unfortunately, it seems that there are no prominent peaks which can differentiate the spectra for the varying uranium enrichments. However, since this has already been shown to be easily performed with the first energy group, it is not necessary for this group.

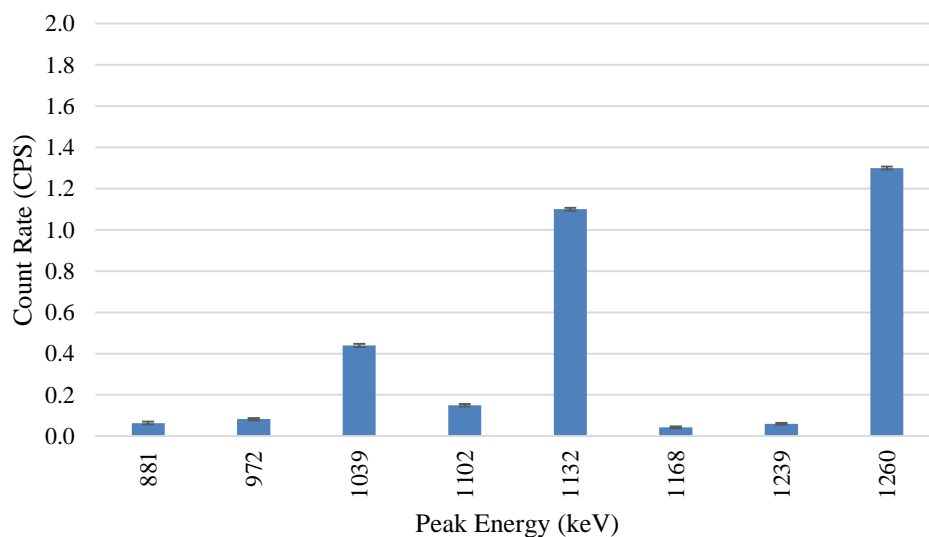


Figure 27. Peaks identified in Genie for the third analyzed energy group of the 20%-enriched uranium fallout spectrum.

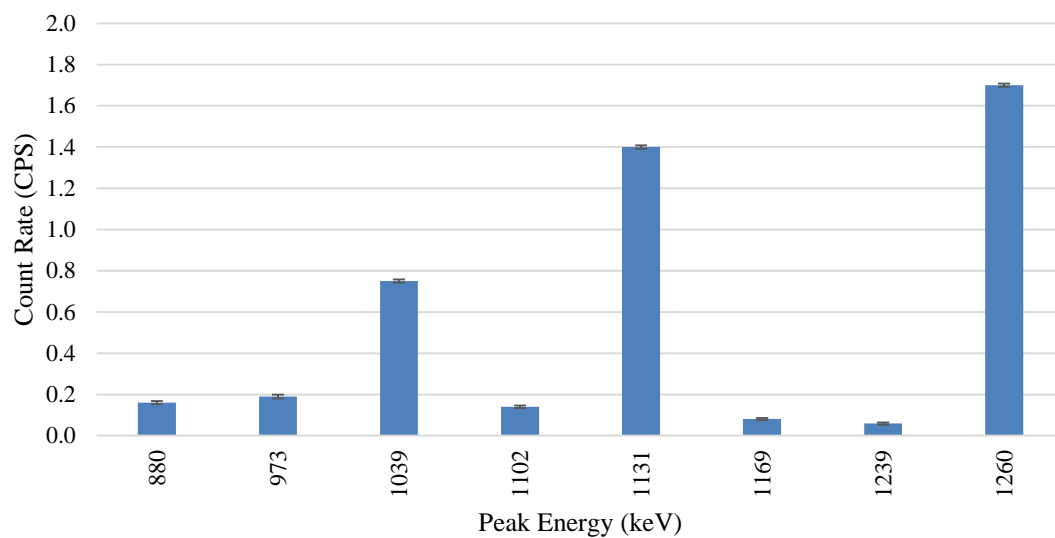


Figure 28. Peaks identified in Genie for the third analyzed energy group of the 50%-enriched uranium fallout spectrum.

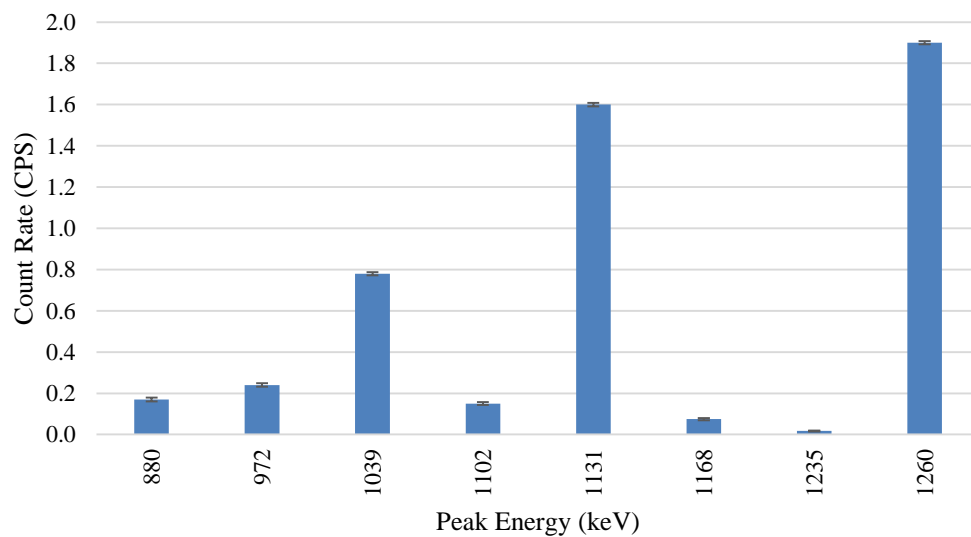


Figure 29. Peaks identified in Genie for the third analyzed energy group of the 90%-enriched uranium fallout spectrum.

The peaks identified in the third energy group of the fallout spectra for reactor-grade and weapons-grade plutonium are displayed in Figure 30 and Figure 31, respectively. It seems that from this group, it is difficult to make any confident distinctions between the two plutonium spectra, or between the plutonium and uranium spectra. The peak heights seem fairly consistent amongst the five spectra. The high-energy peaks begin to make spectroscopy difficult due to the low detection efficiencies at these high energies.

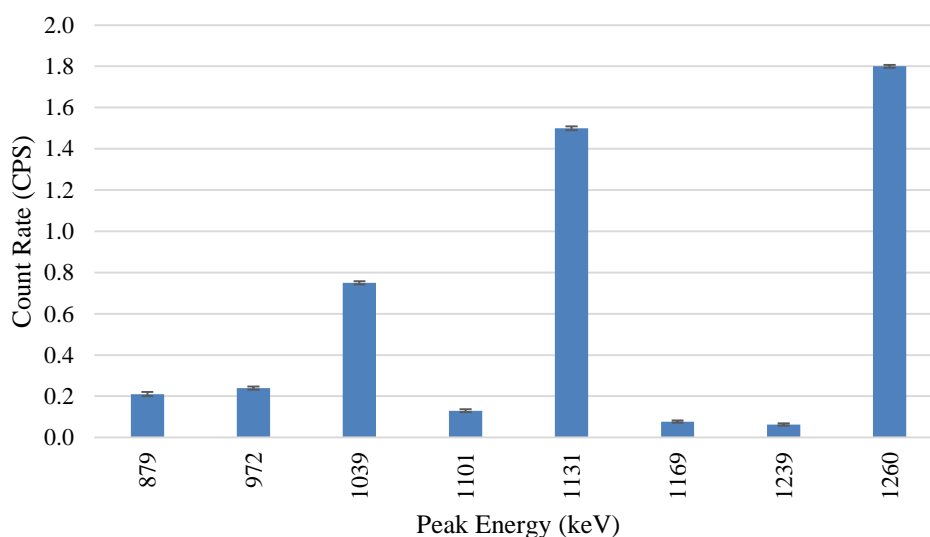


Figure 30. Peaks identified in Genie for the third analyzed energy group of the reactor-grade plutonium fallout spectrum.

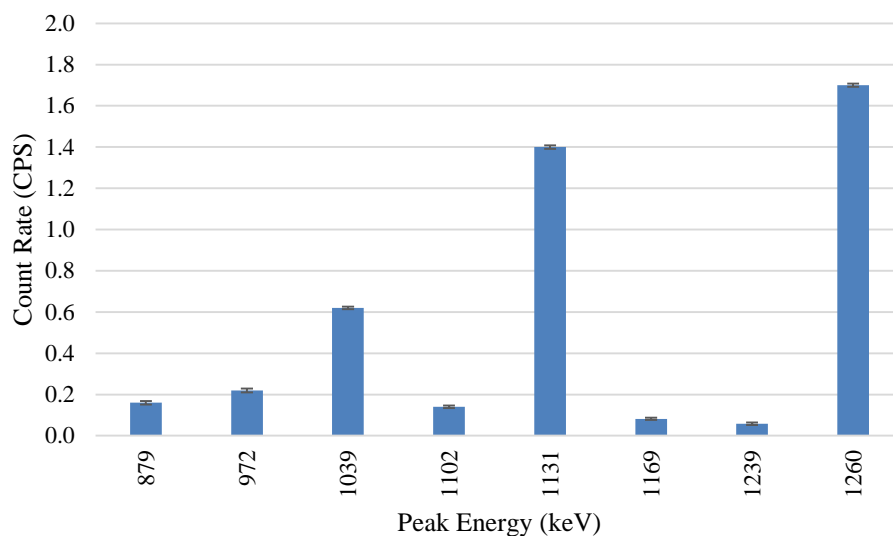


Figure 31. Peaks identified in Genie for the third analyzed energy group of the weapons-grade plutonium fallout spectrum.

3.5 Energy Group 4

The fourth energy group analyzed ranged from 1457 keV to the last peak shared by the spectra, which was located at 1926 keV. Many peaks were dropped due to large relative errors. Since the ability to distinguish between uranium enrichments as well as the ability to distinguish between uranium and plutonium fallout spectra has already been effectively displayed for previous energy groups, the peaks identified in the uranium spectra will not be presented. The peaks identified for this fourth energy group within the reactor-grade plutonium and weapons-grade plutonium spectra are displayed in Figure 32 and Figure 33, respectively.

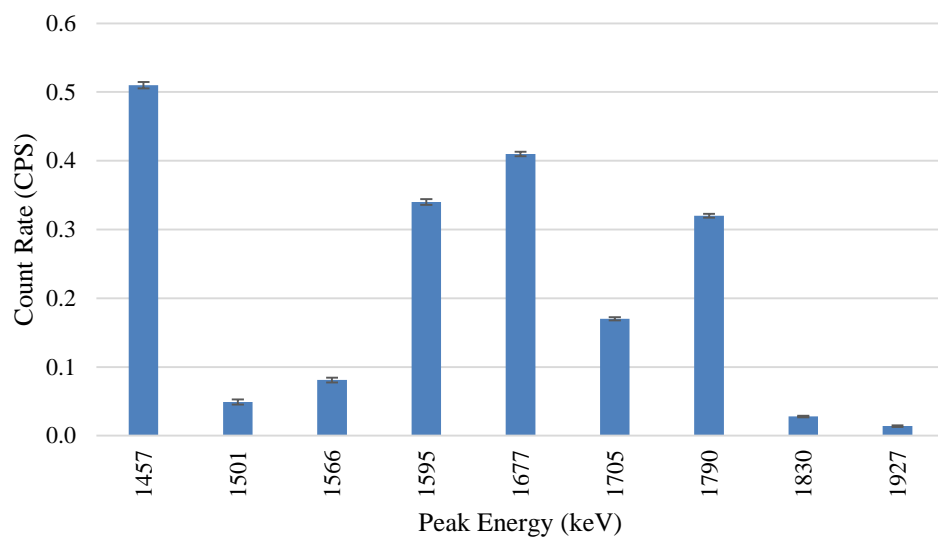


Figure 32. Peaks identified in Genie for the fourth analyzed energy group of the reactor-grade plutonium fallout spectrum.

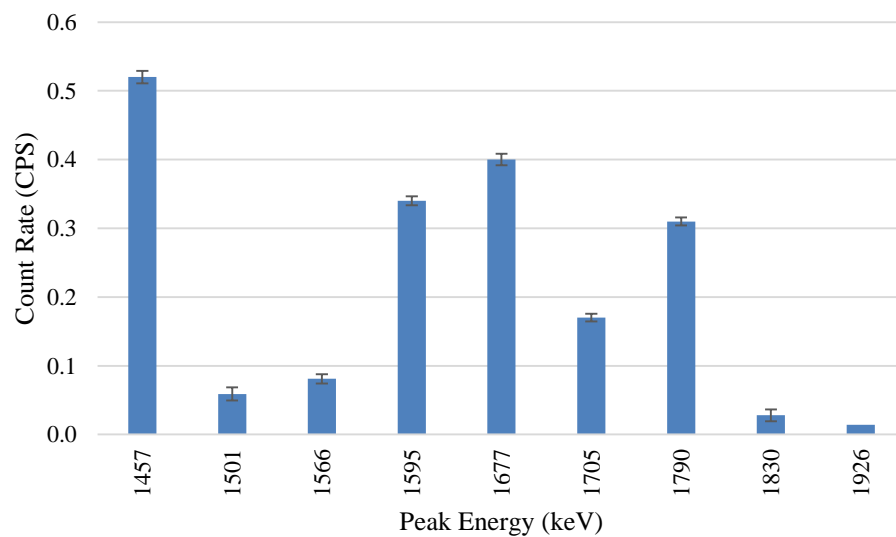


Figure 33. Peaks identified in Genie for the fourth analyzed energy group of the weapons-grade plutonium fallout spectrum.

The ability to distinguish between the fallout spectra of reactor-grade and weapons-grade plutonium still has yet to be identified. In an attempt to see if this was possible, the percent differences between each of the shared peaks throughout the entire energy range from 0 to 2 MeV were calculated. The five peaks with the highest percent differences are displayed in Table 11. The highest difference is 27.0% for the 879 keV peak. This difference still does not seem sufficient to make the assumption that these peaks would be able to be differentiated in the field when incorporating uncertainty within this analysis as well as experimental error when the true measurement is obtained. Therefore, it seems that differentiation between the fallout spectra of reactor-grade and weapons-grade plutonium utilizing a high-purity germanium detector for rapid forensics is not feasible according to this analysis.

Table 11. Peaks with the largest percent differences for reactor-grade and weapons-grade plutonium.

Peak Energy (keV)	Reactor-Grade Plutonium Counts per Second	Weapons-Grade Plutonium Counts per Second	% Difference
778	$0.39 \pm 2.1\%$	$0.33 \pm 2.5\%$	16.7
817	$0.22 \pm 4.7\%$	$0.27 \pm 3.7\%$	20.4
879	$0.21 \pm 4.8\%$	$0.16 \pm 5.6\%$	27.0
1039	$0.75 \pm 1.0\%$	$0.62 \pm 1.1\%$	19.0
1501	$0.049 \pm 7.5\%$	$0.059 \pm 7.5\%$	18.5

3.6 Other Spectral Features

Of the high-energy photons which are present on the spectra, none seem to have sufficiently-high activities in order to cause an additional single escape or double escape

peak which would be also noticeable on the spectrum. These escape peaks are present, but cannot be resolved due to their extremely low occurrence rate. The only two peaks with activities above a single count per second on the spectra are the 1131 keV and 1260 keV peaks. This means that there would be single escape peaks noticeable at 620 keV and 749 keV, respectively, and double escape peaks at 109 keV and 238 keV, respectively. There are no 620 keV or 749 keV peaks noticeable on any of the spectra. Furthermore, there are no 238 keV peaks noticeable on the spectra, and the 109 keV double escape peak is clouded by the large peak at almost the same energy from ^{239}Np .

An annihilation peak would be present at 511 keV. The only spectrum with a peak near this energy is the reactor-grade plutonium fallout spectrum with a peak at 510 keV with a count rate of 0.05 ± 0.01 counts per second. However, since there are no materials or shielding surrounding the detector, this peak is most likely not an annihilation peak. Furthermore, since shielding is not present around the detector, there will likely be no backscatter peak as well.

The Compton edge energy can be calculated for a photon from Eq. (1) with $\theta = \pi$. This Compton edge value for the 108 keV and 251 keV peaks are 32 keV and 124 keV, respectively. A very small peak near 32 keV is present on the 20%-enriched uranium fallout spectrum which is likely the Compton edge, since no other photons are emitted at this energy with sufficiently-high activities to be responsible. Peaks are present in the other four spectra near 34 keV, which may be due to an X-ray from ^{140}Ba . Although the true emission energy of this photon is 29.97 keV, this is being identified at

34 keV by Genie due to a slight overestimation by the energy calibration curve at lower energies.¹⁶ There are no peaks identified near 124 keV for any of the five spectra.

3.7 Issues with Differentiating Reactor-Grade and Weapons-Grade Plutonium

Unfortunately, it seems that analysis of the fallout spectra within Excel and Genie did not produce a viable methodology to differentiate between reactor-grade and weapons-grade plutonium. Figure 34 displays the fission yield data for ^{235}U and ^{238}U for fissions induced with 500 keV neutrons. 500 keV is close to the average neutron energy causing fission in these simulations (the values of which can be found in Table 3).²⁶

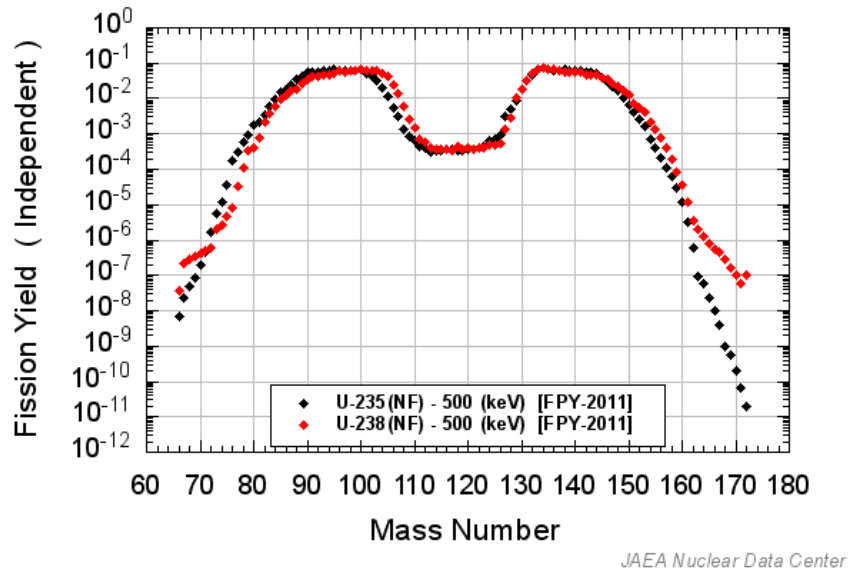


Figure 34. Fission yield data for ^{235}U and ^{238}U for 500 keV neutrons.²⁶

Upon analysis of Figure 34, it is evident that there are several regions of the plot where the fission yields differentiate significantly, including between mass numbers of approximately 75 and 80, again between mass numbers of 105 and 110, and finally

beyond mass numbers of 160. This allows for variations in the fission product concentrations of the fallout which can be used in spectroscopy. However, when the fission yield data of various plutonium isotope are compared, the plots are extremely similar. Figure 35 displays the fission yield data for ^{239}Pu and ^{240}Pu for 500 keV neutrons, while Figure 36 displays the fission yield data for ^{239}Pu and ^{241}Pu for 500 keV neutrons. According to Table 2, it can be seen that the ratio of ^{240}Pu and ^{241}Pu fissions to that of ^{239}Pu fissions has increased from 2.9% and 0.4%, respectively, in weapons-grade plutonium to 25% and 20%, respectively, in reactor-grade plutonium. Despite these differences, the similarity in fission yields from these two isotopes has led to extremely similar photon spectra. Figure 44 in Appendix C contains the fission yield data for ^{239}Pu and ^{238}Pu for 500 keV neutrons, while Figure 45, also in Appendix C, contains the fission yield data for ^{239}Pu and ^{242}Pu for 500 keV neutrons. From these figures, it is also apparent that only minor differences are present between the fission yields of these isotopes.

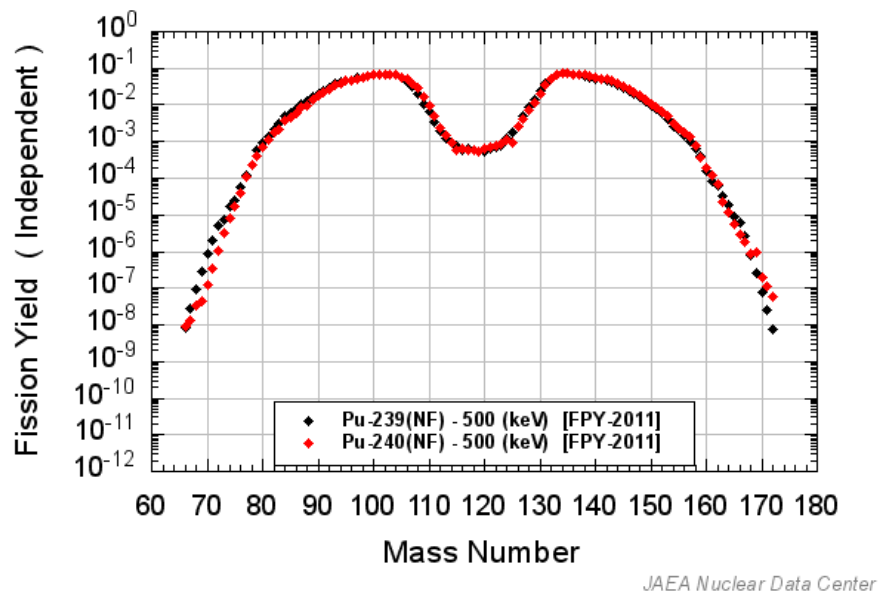


Figure 35. Fission yield data for ^{239}Pu and ^{240}Pu for 500 keV neutrons.²⁶

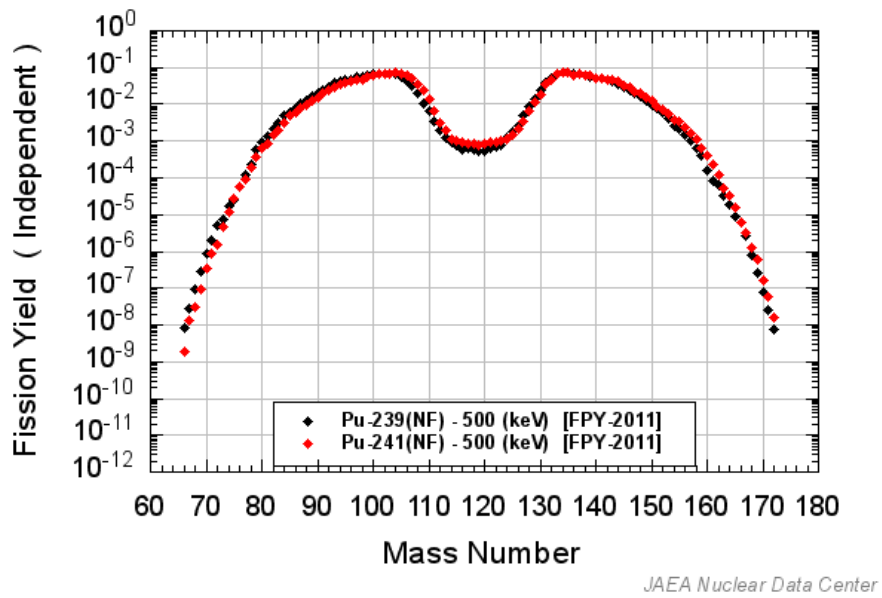


Figure 36. Fission yield data for ^{239}Pu and ^{241}Pu for 500 keV neutrons.²⁶

Figure 37 displays the fission yield data for ^{235}U and ^{239}Pu for 500 keV neutrons. There are large differences apparent between mass numbers of 100 and 130 as well as above 150. This allows for variations in fallout composition and therefore different photon spectra. These variations were not present between the plutonium isotopes, and therefore this presents a large problem when attempting to perform gamma spectroscopy on the fallout.

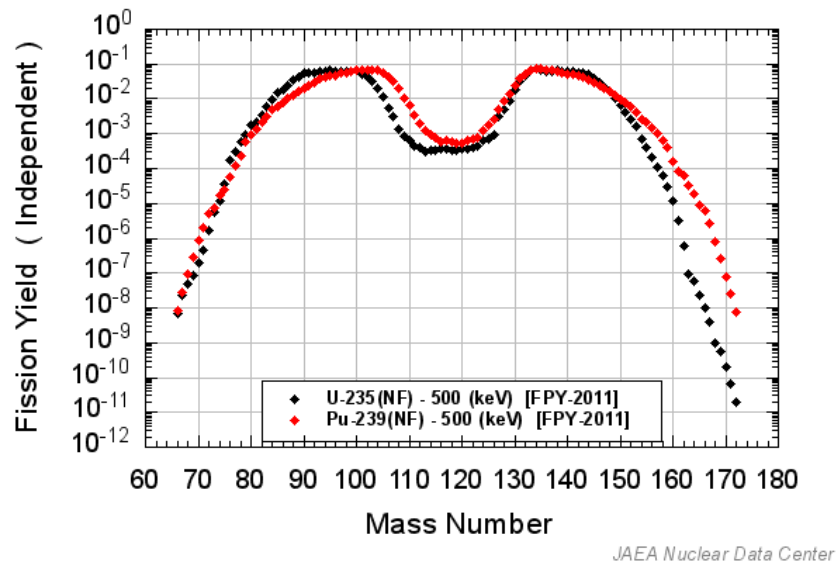


Figure 37. Fission yield data for ^{239}Pu and ^{235}U for 500 keV neutrons.²⁶

3.8 Determination of Initial Weapon Loading: A Flowchart

Based on the previous data, a flowchart can be constructed which depicts the methodology which would be utilized to determine the initial fissile material composition following the acquisition of a photon spectrum on fallout approximately 24 hours post-detonation. This flowchart is depicted in Figure 38.

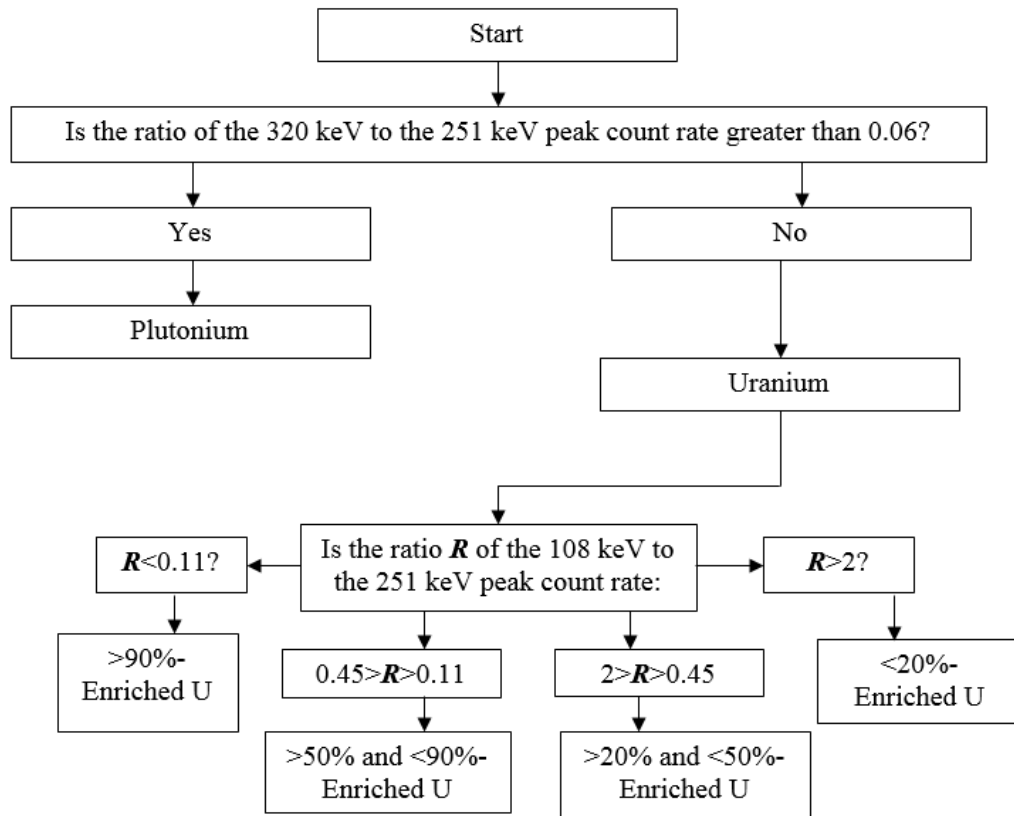


Figure 38. Flowchart to determine initial fissile material content. All ratio values are approximate.

If a more precise estimate for initial uranium enrichment is desired within the range of 20% to 90%, the initial uranium enrichment (in percent) can be estimated by

$$\% \text{ Initial Uranium Enrichment} = 30.0 \cdot R^{-0.52}, \quad (7)$$

where R is the ratio of the 108 keV to 251 keV peak count rate. This equation should be used with cautiousness and an understanding of its limitations. Only 3 data points are utilized to predict its behavior and therefore the uncertainties associated with its predictions may be fairly high.

4. CONCLUSIONS

This analysis has displayed the theoretical capability to distinguish between the fallout of a plutonium and uranium nuclear weapon 24 hours after detonation using a HPGe semiconductor detector. Furthermore, the ability to distinguish between several different enrichments of uranium has been identified. MCNP6 was an effective tool at simulating the detonation of several nuclear weapons, each with a significantly different initial fissile material loading. Using data from online databases and the resulting isotopics of the burn runs, photon source terms for each of the fallout distributions were generated. A HPGe detector was then modeled in MCNP6 to simulate the predicted response functions from photon transport calculations with these source terms. Genie photon analysis software was then utilized to identify peak areas and calculate ratios to differentiate between the spectra.

These abilities could prove to be crucial to the Department of Homeland Security following the devastating event of a nuclear detonation within the United States. This analysis has displayed the ability to discern several types of initial fissile material loadings in-the-field in as little as 24 hours. In doing so, Washington can make more rapid decisions of the necessary corrective actions with the confidence that the data it is receiving is reliable.

4.1 Future Work

Additional work could focus on completing this analysis for additional data points. This includes additional enrichments of uranium, such as in increments of 5%

from 20% to 90%. It should be noted that construction of a nuclear weapon with an enrichment of less than 20% ^{235}U is not feasible and weapons with enrichments of above 90% are extremely rare. The resulting data could be used to improve upon Eq. (7) to predict initial uranium enrichment.

Generating spectra for the fallout of weapons with additional plutonium compositions may lead to a method to distinguish them; however, this seems unlikely due to the failure to do so for the two compositions in this analysis which were already composed of fairly different isotopes. Furthermore, the composition of plutonium in this analysis would be very similar to those which would be utilized in a weapon. Therefore, further investigation into differentiating initial plutonium isotopes with gamma spectroscopy may prove to be unproductive. Other analysis tools may be needed such as in-the-field alpha spectroscopy.

Since the ultimate goal of this analysis is to incorporate the HPGe detector onto an autonomous robotic detection system, future work could focus on modeling this system in the photon transport model of MCNP6 to see how the predicted response function would change. As will be discussed in the next section, it is not expected that it will change significantly.

4.2 Sources of Error

Various assumptions were made throughout this process which will contribute to error and uncertainty associated with the resulting data. The geometry of much of the HPGe detector, including the endcap, casing, and electronics was neglected. In addition, the autonomous robot which will be present on this detection system was not modeled.

This systematic error will lead to additional photon scattering which could contribute to background in the spectra. While addition of these features may change the spectra slightly, it is highly unlikely that this will impact the overall conclusions of the analysis since the primary photopeaks used for differentiation of compositions will still be prominent and easily identified by basic spectroscopy software such as Genie. These scattered photons will typically appear in the Compton continuum or as background, which are both subtracted out by Genie analysis algorithms when performing peak identification. Thus, it only contributes to error in the peaks. While low-energy gammas will be scattered preferentially to higher-energy gammas, the small thickness of detector endcaps will likely minimize this impact.

The GEB parameters were calculated with data obtained from a paper describing a different HPGe detector than the one modeled. Since both of the detectors are high-purity germanium crystals, this detail is not expected to impact the results significantly.

There was assumed to be no variation in the isotopic distribution of the fallout. This is likely the largest source of error within this investigation. However, as discussed previously, calculations which incorporate variations in the isotopic distribution of fallout are likely not any more accurate than calculations which simply ignore them, and therefore neglecting them is justifiable at this time. Improvements in modeling capabilities for these fractionation effects or choices of radionuclides with similar geochemistry is advised.

To model the source from the soil contamination on the ground, a 1 m² source was assumed. To make the model more like reality, the source should be modeled as a

plane with a much larger surface area (on the order of several square miles). This would be inefficient to model in MCNP and lead to results with very high relative errors. In addition, in a true scenario buildings or rubble would be present which would shield much of the photon activity and this is difficult to predict and model in MCNP. It is expected that the response function from this source will be extremely similar to one from a significantly-larger plane with the same source definition.

An additional source of error may be the assumed weapon detonation time. However, earlier calculations displayed that changing this detonation time did not impact results since the burnup was maintained to be constant and no nuclide decay occurred at this short time scale. Therefore, the error associated with this assumption is judged to be negligible.

In a real-life scenario, the composition of the materials such as the soil and air will not be identical to that which was modeled in this calculation. However, the error associated with this assumption is expected to be small since any variations in these compositions should not significantly impact photon transport calculations.

In any Monte Carlo calculation, there is an uncertainty associated with any result due to the nature of counting statistics. This is called statistical, or random error, in contrast to systematic error. This uncertainty could be decreased to zero with an infinite number of trials; however, this is impossible within a finite time. Therefore, a level of precision must be chosen to be acceptable. Since much of this analysis was completed with MCNP6, the spectra, ratios, isotopics, and all other MCNP6-generated values will have statistical uncertainties. However, it was shown before that increasing the number

of burnup steps did not change the resulting isotopics by a significant amount, and therefore values with three steps were considered to be sufficiently precise.

In the photon transport simulation in MCNP6, the boundary of the problem was assumed to be 500 cm away from the origin. While in reality some photons may exit this boundary and be scattered back in and be detected, this is extraordinarily unlikely and its impact on results will be negligible.

REFERENCES

- ¹ Knoll, G. F. (2010). *Radiation Detection and Measurement*. New York: Wiley.
- ² University of New South Wales. (2003). Solar Cells: Resources for the Secondary Science Teacher. Sydney. Key Centre for Photovoltaic Engineering, faculty of Engineering.
- ³ Kalos, Malvin H., & Whitlock, Paula A. (2008). *Monte Carlo Methods*. Wiley-VCH Verlag GmbH & Co. KGaA, Weinheim.
- ⁴ Los Alamos National Laboratory. (2008). Monte Carlo N-Particle Transport Code, Version 6. Los Alamos.
- ⁵ Los Alamos National Laboratory. (2008). MCNP6 User's Manual. Los Alamos.
- ⁶ Fensin, M. (2008). Development of the MCNPX Depletion Capability: A Monte Carlo Linked Depletion Method that Automates the Coupling Between MCNPX and CINDER90 for High Fidelity Burnup Calculations. The University of Florida.
- ⁷ Buragohain, M., Venayagamoorthy, G. K., & Tokuhito, A. (2004). Development of an Autonomous Mobile Robot for Radiation Source Detection using Neural Networks. Faculty Research & Creative Works. Artificial Neural Networks in Engineering Conference, 2004 (pp. 385-390). St. Louis: American Society of Mechanical Engineers.
- ⁸ Qian, K., Song, A., Bao, J., & Zhang, H. (2012). Small Teleoperated Robot for Nuclear Radiation and Chemical Leak Detection. *International Journal of Advanced Robotic Systems*, 9, 1-9.
- ⁹ Towler, J., Krawiec, B., & Kochersberger, K. (2012). Radiation Mapping in Post-Disaster Environments Using an Autonomous Helicopter. *Remote Sensing*, 4, 1995-2015.
- ¹⁰ Pollanen, R., Toivonen, H., Perajarvi, K., Karhunen, T., Smolander, P., Ilander, T., . . . Palos, T. (2009). Performance of an air sampler and a gamma-ray detector in a small unmanned aerial vehicle. *Journal of Radioanalytical and Nuclear Chemistry*, 282, 433-437.
- ¹¹ Pollanen, R., Toivonen, H., Perajarvi, K., Karhunen, T., Smolander, P., Ilander, T., . . . Palos, T. (2009). Radiation Surveillance using an Unmanned Aerial Vehicle. *Applied Radiation and Isotopes*, 67, 340-344.

- ¹² Kurvinen, K., Smolander, P., Pollanen, R., Kuukankorpi, S., Kettunen, M., & Lyytinen, J. (2005). Design of a Radiation Surveillance Unit for an Unmanned Aerial Vehicle. *Journal of Environmental Radioactivity*, 81, 1-10.
- ¹³ Fahey, A. J., Zeissler, C. J., Newbury, D. E., Davis, J., & Lindstrom, R. M. (2010). Postdetonation Nuclear Debris for Attribution. *Proceedings of the National Academy of Sciences of the United States of America*, 107, 20207–20212.
- ¹⁴ Foster, K., & Krauss, T. (2013). Analysis of Fission and Activation Radionuclides Produced by the Detonation of a Uranium-Fueled Improvised Nuclear Device and Identification of the Top Dose-Producing Radionuclides. Livermore: Sandia National Laboratory/Lawrence Livermore National Laboratory.
- ¹⁵ Department of Homeland Security. (2006). *National Planning Scenarios*. Washington, D.C.
- ¹⁶ Korea Atomic Energy Research Institute. (2015, February 8). Table of Nuclides. Retrieved from <http://atom.kaeri.re.kr/>.
- ¹⁷ International Atomic Energy Agency. (1997). Plutonium Isotopics - Non-Proliferation And Safeguards Issues. *IAEA Symposium on International Safeguards*, 30, pp. 13-17. Vienna.
- ¹⁸ Lamarsh, J., & Baratta, A. (2001). *Introduction to Nuclear Engineering*. Upper Saddle River: Prentice Hall.
- ¹⁹ National Nuclear Data Center of Brookhaven National Laboratory. (2015). NuDat. Upton.
- ²⁰ LeJeune, J. (2014, October). Account Manager, CANBERRA. Personal Communication. (S. Horowitz, Interviewer).
- ²¹ Shepard, H. (2014, October). Technical Support, CANBERRA. Personal Communication. (S. Horowitz, Interviewer).
- ²² Burks, M. (2008). GeMini: The Next-Generation Mechanically-Cooled Germanium Spectrometer. *IEEE Nuclear Science Symposium Conference Record* (pp. 1375-1377). Dresden: Institute of Electrical and Electronics Engineers.
- ²³ Free Software Foundation, Inc. Xming. (1991). Boston.
- ²⁴ Pacific Northwest National Laboratory. (2011). *Compendium of Material Composition Data for Radiation Transport Modeling*. Alexandria.

²⁵ Canberra Industries. (2009). GENIE-2000 InSpector Basic Spectroscopy V3.2.1. Meriden.

²⁶ Japan Atomic Energy Agency. (2015). Graph of Fission Product Yields. Nuclear Data Center, Tokai-mura, Naka-gun, Ibaraki-ken, Japan. Retrieved from <http://www.ndc.jaea.go.jp/cgi-bin/FPYfig?mode=m&iso=nPu238&iso=nPu239&eng=e3&iso=nPu240&iso=nPu241&iso=nPu242&eng=e11>.

APPENDIX A

FISSION PRODUCTS TRACKED IN MCNP6

Table 12. Tier-3 fission products tracked in MCNP6.⁵

Gallium-69	Zirconium-93	Cadmium-110	Iodine-135	Praseodymium-143	Dysprosium-158
Gallium-71	Zirconium-94	Cadmium-111	Xenon-123	Neodymium-142	Dysprosium-160
Germanium-70	Zirconium-95	Cadmium-112	Xenon-124	Neodymium-143	Dysprosium-161
Germanium-72	Zirconium-96	Cadmium-113	Xenon-126	Neodymium-144	Dysprosium-162
Germanium-73	Niobium-93	Cadmium-114	Xenon-128	Neodymium-145	Dysprosium-163
Germanium-74	Niobium-94	Cadmium-116	Xenon-129	Neodymium-146	Dysprosium-164
Germanium-76	Niobium-95	Indium-113	Xenon-130	Neodymium-147	Holmium-165
Arsenic-74	Molybdenum-92	Indium-115	Xenon-131	Neodymium-148	Erbium-162
Arsenic-75	Molybdenum-94	Tin-112	Xenon-132	Neodymium-150	Erbium-164
Selenium-74	Molybdenum-95	Tin-113	Xenon-133	Promethium-147	Erbium-166
Selenium-76	Molybdenum-96	Tin-114	Xenon-134	Promethium-148	Erbium-167
Selenium-77	Molybdenum-97	Tin-115	Xenon-135	Promethium-149	Erbium-168
Selenium-78	Molybdenum-98	Tin-116	Xenon-136	Promethium-151	Erbium-170
Selenium-79	Molybdenum-99	Tin-117	Cesium-133	Samarium-144	Thulium-169
Selenium-80	Molybdenum-100	Tin-118	Cesium-134	Samarium-147	
Selenium-82	Technetium-99	Tin-119	Cesium-135	Samarium-148	
Bromine-79	Ruthenium-96	Tin-120	Cesium-136	Samarium-149	
Bromine-81	Ruthenium-98	Tin-122	Cesium-137	Samarium-150	
Krypton-78	Ruthenium-99	Tin-123	Barium-130	Samarium-151	
Krypton-80	Ruthenium-100	Tin-124	Barium-132	Samarium-152	
Krypton-82	Ruthenium-101	Tin-125	Barium-133	Samarium-153	
Krypton-83	Ruthenium-102	Tin-126	Barium-134	Samarium-154	
Krypton-84	Ruthenium-103	Antimony-121	Barium-135	Europium-151	
Krypton-85	Ruthenium-104	Antimony-123	Barium-136	Europium-152	
Krypton-86	Ruthenium-105	Antimony-124	Barium-137	Europium-153	
Rubidium-86	Ruthenium-106	Antimony-125	Barium-138	Europium-154	
Rubidium-87	Rhodium-103	Antimony-126	Barium-140	Europium-155	
Strontium-84	Rhodium-105	Tellurium-120	Lanthanum-138	Europium-156	
Strontium-86	Palladium-102	Tellurium-122	Lanthanum-139	Europium-157	
Strontium-87	Palladium-104	Tellurium-123	Lanthanum-140	Gadolinium-152	
Strontium-88	Palladium-105	Tellurium-124	Cerium-136	Gadolinium-153	
Strontium-89	Palladium-106	Tellurium-125	Cerium-138	Gadolinium-154	
Strontium-90	Palladium-107	Tellurium-126	Cerium-139	Gadolinium-155	
Yttrium-88	Palladium-108	Tellurium-128	Cerium-140	Gadolinium-156	
Yttrium-89	Palladium-110	Tellurium-130	Cerium-141	Gadolinium-157	
Yttrium-90	Silver-107	Tellurium-132	Cerium-142	Gadolinium-158	
Yttrium-91	Silver-109	Iodine-127	Cerium-143	Gadolinium-160	
Zirconium-90	Silver-111	Iodine-129	Cerium-144	Terbium-159	
Zirconium-91	Cadmium-106	Iodine-130	Praseodymium-141	Terbium-160	
Zirconium-92	Cadmium-108	Iodine-131	Praseodymium-142	Dysprosium-156	

APPENDIX B

RELATIVE ERRORS FOR PHOTON SPECTRA

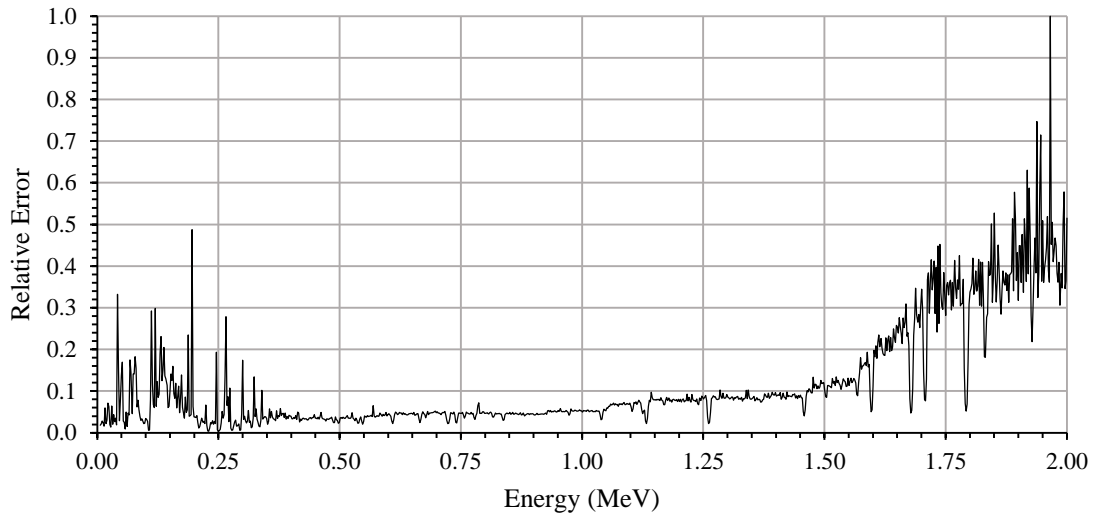


Figure 39. Relative errors for the 20%-enriched uranium spectra.

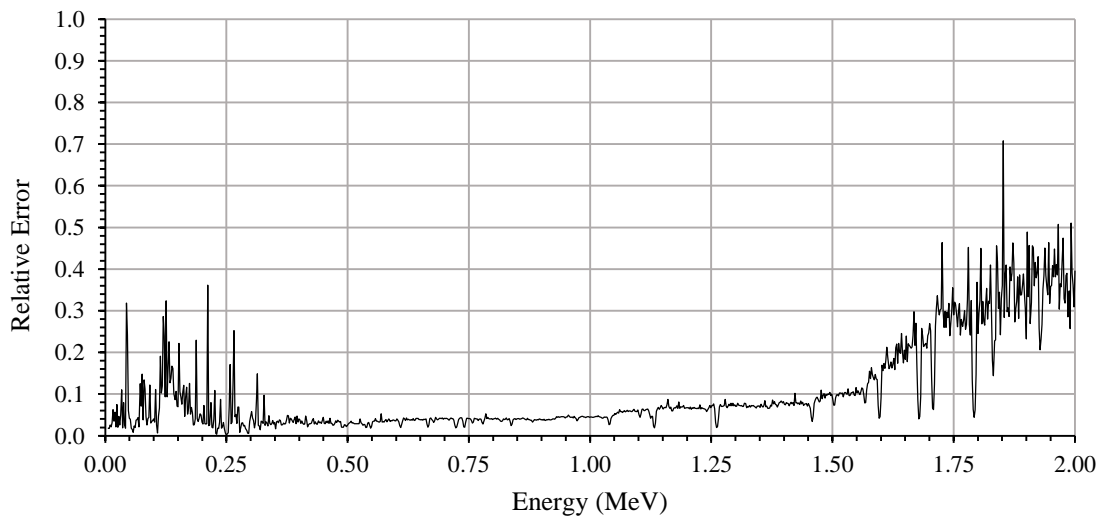


Figure 40. Relative errors for the 50%-enriched uranium spectra.

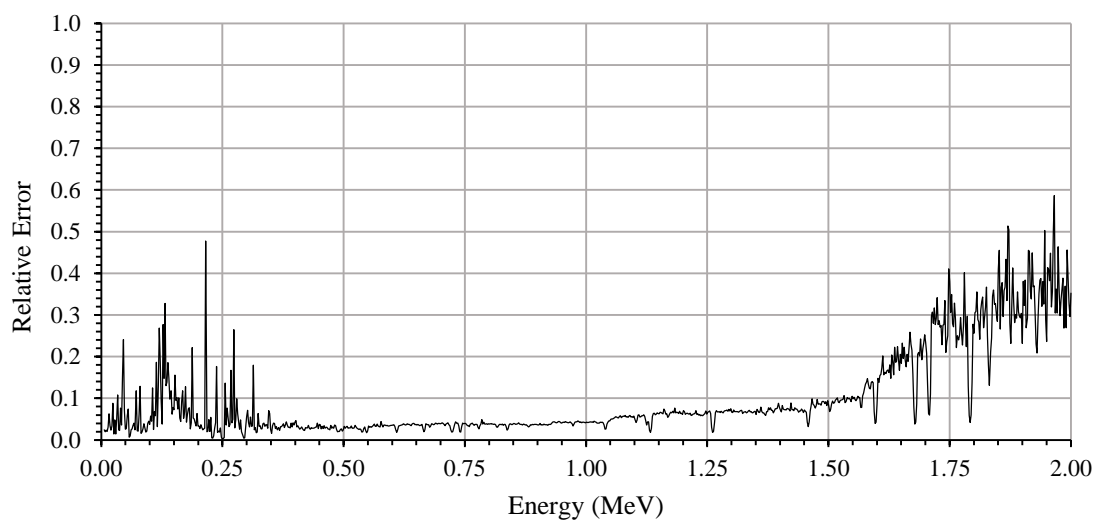


Figure 41. Relative errors for the 90%-enriched uranium spectra.

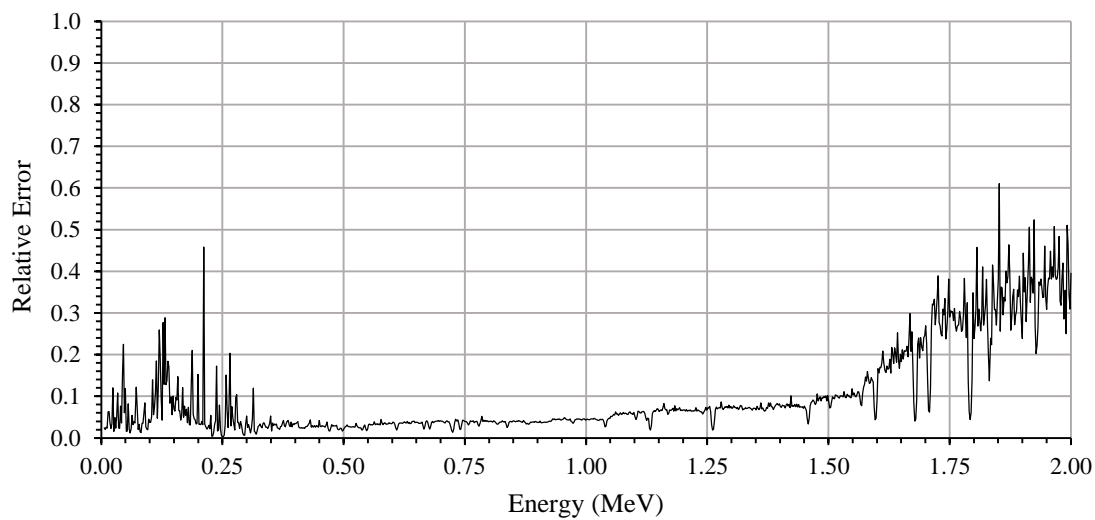


Figure 42. Relative errors for the reactor-grade plutonium fallout spectra.

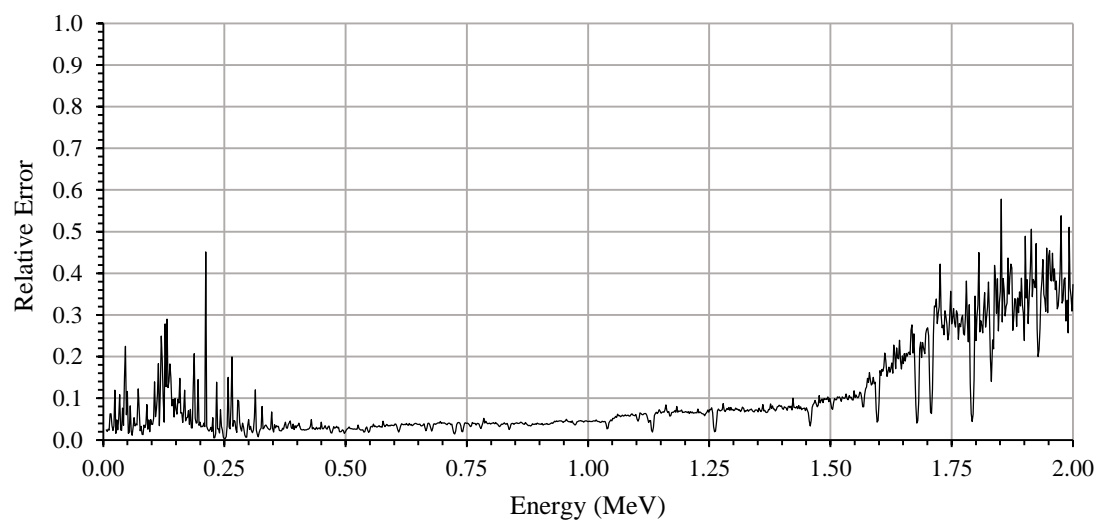


Figure 43. Relative errors for the weapons-grade plutonium fallout spectra.

APPENDIX C

ADDITIONAL FISSION YIELD DATA

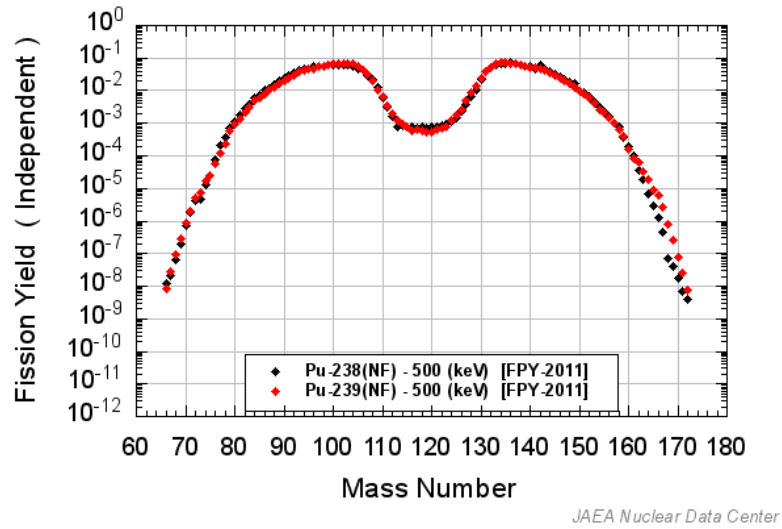


Figure 44. Fission yield data for ^{238}Pu and ^{239}Pu for 500 keV neutrons.²⁶

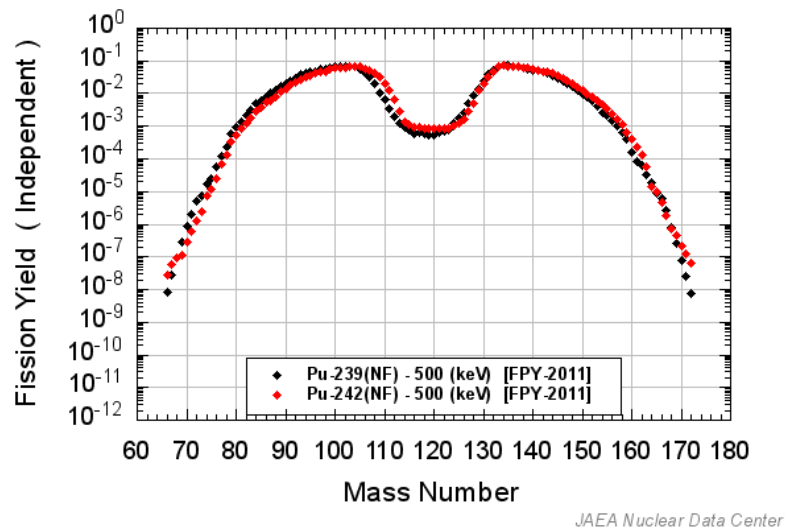


Figure 45. Fission yield data for ^{239}Pu and ^{242}Pu for 500 keV neutrons.²⁶

MCNP6 BURNUP DECK FOR 20%-ENRICHED URANIUM

c

4567890123456789012345678901234567890123456789012345678901234
567890

```
c ccccccccc Cell Cards cccccccccccccccccccccccccccccccccc
1    1 -18.9 -1   imp:n=1  VOL = 65449.85   $ Sphere at origin
2    0    +1   imp:n=0                $ Graveyard
```

```
c cccccccccc Surface Cards cccccccccccccccccccccccccccccccc
c      -- HPGe detector --
1  so 25.00      $ U Sphere
```

```
MODE n
kcode 5000 1.0 10 100
ksrc 0 0 0
```

$$\begin{array}{r} 1\ 1\ 1 \\ 2\ 2\ 2 \\ -1\ -1\ -1 \\ -5\ -5\ -5 \\ 5\ 5\ 5 \\ 7\ 7\ 7 \\ -7\ -7\ -7 \\ -2\ 2\ 1 \\ 2\ 5\ -1 \\ 8\ -5\ 3 \end{array}$$

```

BURN  TIME = 3.85417e-8 3.85417e-8 3.85417e-8 1
      PFRAC = 1.0 1.0 1.0 0
      MAT = 1
      POWER = 4.184E9
      MATVOL = 65449.85
      BOPT= 1.0 24 -1
      OMIT = 1 161
      29066  $Copper-66
      30069  $Zinc-69
      31070  $Gallium-70
      32071  $Germanium-71
      32075  $Germanium-75

```

33072	\$Arsenic-72
33073	\$Arsenic-73
34075	\$Selenium-75
34081	\$Selenium-81
35080	\$Bromine-80
36079	\$Krypton-79
36081	\$Krypton-81
37083	\$Rubidium-83
38085	\$Strontium-85
38085	\$Strontium-85
39086	\$Yttrium-86
39087	\$Yttrium-87
39092	\$Yttrium-92
39093	\$Yttrium-93
40088	\$Zirconium-88
40089	\$Zirconium-89
40097	\$Zirconium-97
41091	\$Niobium-91
41092	\$Niobium-92
41096	\$Niobium-96
41097	\$Niobium-97
41098	\$Niobium-98
41099	\$Niobium-99
41100	\$Niobium-100
42091	\$Molybdenum-91
42093	\$Molybdenum-93
42101	\$Molybdenum-101
43097	\$Technetium-97
43098	\$Technetium-98
44097	\$Ruthenium-97
45104	\$Rhodium-104
45106	\$Rhodium-106
45107	\$Rhodium-107
45108	\$Rhodium-108
45109	\$Rhodium-109
45110	\$Rhodium-110
45111	\$Rhodium-111
46103	\$Palladium-103
46109	\$Palladium-109
46111	\$Palladium-111
46112	\$Palladium-112
46113	\$Palladium-113
46114	\$Palladium-114
47106	\$Silver-106

47108	\$Silver-108
47110	\$Silver-110
48107	\$Cadmium-107
48109	\$Cadmium-109
48115	\$Cadmium-115
49114	\$Indium-114
49116	\$Indium-116
49117	\$Indium-117
49118	\$Indium-118
49119	\$Indium-119
49121	\$Indium-121
49122	\$Indium-122
49123	\$Indium-123
49124	\$Indium-124
50121	\$Tin-121
51122	\$Antimony-122
52121	\$Tellurium-121
52127	\$Tellurium-127
52129	\$Tellurium-129
53128	\$Iodine-128
53132	\$Iodine-132
53133	\$Iodine-133
53134	\$Iodine-134
54125	\$Xenon-125
54127	\$Xenon-127
56131	\$Barium-131
58137	\$Cerium-137
59145	\$Praseodymium-145
60149	\$Neodymium-149
61145	\$Promethium-145
61146	\$Promethium-146
62145	\$Samarium-145
62146	\$Samarium-146
64150	\$Gadolinium-150
64151	\$Gadolinium-151
64159	\$Gadolinium-159
66157	\$Dysprosium-157
66159	\$Dysprosium-159
67163	\$Holmium-163
67164	\$Holmium-164
67166	\$Holmium-166
68163	\$Erbium-163
68165	\$Erbium-165
68169	\$Erbium-169

69166	\$Thulium-166
69167	\$Thulium-167
69171	\$Thulium-171
69172	\$Thulium-172
69173	\$Thulium-173
70168	\$Ytterbium-168
70169	\$Ytterbium-169
70170	\$Ytterbium-170
70171	\$Ytterbium-171
70172	\$Ytterbium-172
70173	\$Ytterbium-173
70174	\$Ytterbium-174
71173	\$Lutetium-173
88227	\$Radium-227
89228	\$Actinium-228
95239	\$Americium-239
37083	\$Rubidium-83
37084	\$Rubidium-84
55131	\$Cesium-131
80203	\$Mercury-203
81206	\$Thallium-206
81207	\$Thallium-207
81208	\$Thallium-208
81209	\$Thallium-209
82209	\$Lead-209
82210	\$Lead-210
82211	\$Lead-211
82212	\$Lead-212
82214	\$Lead-214
83207	\$Bismuth-207
83208	\$Bismuth-208
83210	\$Bismuth-210
83211	\$Bismuth-211
83212	\$Bismuth-212
83213	\$Bismuth-213
83214	\$Bismuth-214
84209	\$Polonium-209
84210	\$Polonium-210
84211	\$Polonium-211
84214	\$Polonium-214
84215	\$Polonium-215
84216	\$Polonium-216
85210	\$Astatine-210
85211	\$Astatine-211

85212	\$Astatine-212
85213	\$Astatine-213
85214	\$Astatine-214
85215	\$Astatine-215
86211	\$Radon-211
86212	\$Radon-212
86213	\$Radon-213
86214	\$Radon-214
86215	\$Radon-215
86216	\$Radon-216
86217	\$Radon-217
86218	\$Radon-218
86219	\$Radon-219
86220	\$Radon-220
86221	\$Radon-221
86222	\$Radon-222
87221	\$Francium-221
87222	\$Francium-222
87223	\$Francium-223
88222	\$Radium-222
88228	\$Radium-228
89223	\$Actinium-223
89224	\$Actinium-224
93240	\$Neptunium-240
M1 92235.70c 20	\$Uranium-235
92238.70c 80	\$Uranium-238

76

14	pz	-30.0	\$ Top of Contaminated Layer of Soil
15	px	-2.50	\$ Side of Aluminum Window
16	px	2.50	\$ Side of Aluminum Window
17	py	-2.50	\$ Side of Aluminum Window
18	py	2.50	\$ Side of Aluminum Window
19	pz	2.03	\$ Bottom of Aluminum Window
20	pz	2.08	\$ Top of Aluminum Window
99	so	500	\$ Universe

c ccccccccc Data Cards ccccccccccccccccccccccccccccccccc

MODE P

rand seed=15

c ccccccccc Spontaneous Photon Source ccccccccccccccccc

SDEF PAR=2 ERG=D1 POS=0 0 6.53 VEC=0 0 -1 DIR=D2 RAD=D3

SI1 L

0.0000768
0.004821
0.00785
0.00822
0.009365
0.01049
0.012965
0.01381
0.013846
0.0177
0.0184
0.018764
0.01959
0.0198
0.01981296
0.021036
0.021543
0.021646
0.02252
0.0227
0.02328
0.024595
0.02569
0.026348
0.026532
0.029374
0.029966
0.03004
0.03077

0.031444
0.0316
0.033195
0.033568
0.0347
0.0352
0.035489
0.03854
0.038661
0.03872
0.039578
0.03976
0.0405845
0.04098
0.0414
0.04196
0.04206
0.04263
0.042641
0.043423
0.0438
0.04466
0.0452972
0.04621
0.04653
0.04669
0.04756
0.049369
0.04941
0.04955
0.04972
0.05101
0.05122
0.051624
0.051834
0.0532
0.053275
0.053395
0.054039
0.0541
0.0541934
0.05425
0.054548
0.056828

0.057104
0.05728
0.0573
0.057356
0.0579805
0.05903
0.059536
0.05993
0.0600086
0.061
0.06146
0.06185
0.06239
0.06241
0.06259
0.06291
0.06317
0.0639
0.063929
0.064135
0.064281
0.06437
0.0644
0.06483
0.06488
0.06571
0.06583
0.066881
0.067674
0.06786
0.0682557
0.068696
0.06874
0.068916
0.069673
0.0697
0.06976
0.07049
0.0727
0.07298
0.07454
0.07502
0.07542213
0.076073

0.07622
0.076925
0.077592
0.07843
0.079623
0.08012
0.080185
0.080997
0.08102
0.0812
0.08336716
0.0859
0.086062
0.08636
0.086477
0.086545
0.086938
0.087567
0.08799
0.08806
0.0888
0.0889656
0.08948595
0.0895
0.0896
0.0897
0.08973
0.091105
0.0917
0.09297
0.094
0.09464
0.0956
0.0957
0.09609
0.09613
0.09675
0.09675
0.0968825
0.097431
0.0976
0.09805
0.09874
0.09878

0.09949
0.099961
0.10002
0.1006
0.10193
0.101965
0.1027
0.10298
0.10306
0.10318011
0.10484
0.105305
0.106123
0.10615
0.10647
0.1087
0.10916
0.109422
0.10956
0.109681
0.110895
0.11176
0.11275
0.1128
0.1131
0.1131
0.11325
0.1135
0.11351
0.11497
0.11538
0.1154
0.11545
0.11626
0.1163
0.11631
0.116955
0.117702
0.1181117
0.118837
0.1197
0.11972
0.12035
0.12048

0.1209
0.12122
0.12177
0.12235
0.1224
0.123228
0.12362
0.1244
0.12451
0.1249
0.1252
0.1252
0.12521
0.129296
0.1295
0.129782
0.12981
0.13043
0.1311
0.131117
0.131438
0.132687
0.13281
0.133515
0.13422
0.134285
0.1349
0.13655
0.13838
0.1387
0.1389
0.13928
0.13933
0.139742
0.1399
0.140511
0.14076
0.141657
0.1424
0.14317
0.1432
0.143249
0.14335
0.14376

0.144201
0.14544
0.146061
0.146094
0.14753
0.14821
0.1485
0.1491
0.1493
0.15093
0.15118
0.151414
0.1516245
0.153246
0.15337
0.154
0.155239
0.1555
0.15618
0.1581
0.158197
0.15841
0.158782
0.16019
0.1602
0.16032
0.16033
0.160613
0.16145
0.16182
0.16237
0.16241
0.16265
0.16266
0.16294
0.16333
0.16346
0.16358
0.1637
0.16392
0.16461
0.16574
0.16639
0.1665548

0.166576
0.16775
0.16781
0.16839
0.169156
0.17059
0.1709
0.17128
0.171393
0.1723035
0.17256
0.172719
0.17285307
0.1733
0.173543
0.1737
0.17612
0.176314
0.17652
0.176602
0.17716
0.177214
0.178842
0.17922
0.18081
0.181068
0.1817
0.18261
0.1836
0.18449
0.185715
0.18659
0.1869
0.187285
0.18823
0.18936
0.18961
0.19016
0.19146
0.1929
0.19326
0.19494
0.19495
0.1955

0.195679
0.19664
0.19686
0.19719
0.197299
0.1976
0.198654
0.1989
0.199216
0.19995
0.20019
0.20162
0.20196
0.20211
0.2029
0.20329
0.20355
0.20412
0.20412
0.204138
0.20417
0.205311
0.2057
0.2067
0.207
0.208
0.208077
0.20828
0.2086
0.208621
0.209
0.209
0.20919
0.20932
0.209753
0.21031
0.21205
0.21229
0.21401
0.21528
0.2153
0.218
0.220502
0.22138

0.2218
0.2226
0.223234
0.2238
0.22508
0.22542
0.22638
0.22663
0.22718
0.2278
0.22781
0.227891
0.22816
0.228183
0.22878
0.22901
0.22972
0.22994
0.23155
0.23218
0.23243
0.2327
0.2328
0.2335
0.2335
0.2344
0.23569
0.2362
0.2366
0.2367
0.2371
0.23777
0.23786
0.2379
0.24009
0.24087
0.24188
0.24193
0.24208
0.2421
0.24229
0.24338
0.24492
0.24521

0.2454
0.2454
0.2465
0.24684
0.2471
0.2475
0.2478
0.24895
0.24895
0.24903
0.249794
0.2505
0.2523
0.25428
0.25439
0.2544
0.25457
0.25474
0.25488
0.255384
0.25709
0.25811
0.25825
0.25825
0.2614
0.26244
0.26283
0.26323
0.26395
0.26426
0.2657
0.26645
0.266543
0.26754
0.2706
0.27072
0.272498
0.27284
0.2729
0.273646
0.2751
0.27521
0.275374
0.27543

0.27686
0.27709
0.277599
0.27762
0.2782
0.2783
0.2783
0.2784
0.2786
0.27965
0.28009
0.2801
0.2812
0.28124
0.28142
0.28245
0.28292
0.2835
0.284305
0.285
0.2853
0.28546
0.28595
0.2862
0.2863
0.288023
0.288451
0.28956
0.29027
0.29075
0.2914
0.29165
0.29169
0.2924
0.2927
0.2927
0.293266
0.2948
0.29498
0.2952
0.2958
0.2973
0.2973
0.29746

0.2978
0.3017
0.3018
0.3024
0.3024
0.3025
0.3028
0.302853
0.30287
0.30299
0.304849
0.30491
0.30522
0.30583
0.3061
0.30666
0.30674
0.3069
0.30785
0.30897
0.3091
0.3108
0.3108
0.3112
0.3113
0.31178
0.31492
0.31495
0.3151
0.3155
0.31588
0.31641
0.31644
0.3171
0.3173
0.31772
0.318088
0.31871
0.3189
0.319411
0.31968
0.319911
0.320862
0.32104

0.32187
0.3223
0.3224
0.32384
0.32394
0.32395
0.32465
0.3252
0.325789
0.3258
0.326
0.32614
0.32753
0.3283
0.328762
0.329
0.32975
0.33085
0.33182
0.3319
0.3321
0.33236
0.332845
0.3336
0.33431
0.334441
0.33538
0.3358
0.336113
0.33616
0.3377
0.3383
0.3393
0.3394
0.34008
0.340547
0.341
0.341506
0.34213
0.34213
0.34252
0.3433
0.3435
0.34461

0.3449
0.34501
0.345013
0.3459
0.3461
0.3461
0.34827
0.3488
0.34981
0.34996
0.35
0.35018
0.350619
0.35071
0.35095
0.3523
0.35332
0.35346
0.354
0.35603
0.35739
0.3578
0.35839
0.3584
0.3584
0.358931
0.35957
0.3609
0.36185
0.36189
0.36281
0.3635
0.364489
0.366421
0.36656
0.36707
0.368554
0.36859
0.369
0.36945
0.37042
0.370509
0.37094
0.37129

0.37313
0.3742
0.3746
0.37475
0.375054
0.3769
0.3785
0.37986
0.379905
0.38013
0.380191
0.380452
0.3812
0.3814
0.38275
0.38317
0.383851
0.386
0.3866
0.38782
0.38964
0.39067
0.3917
0.3924
0.39253
0.39314
0.39336
0.393408
0.39563
0.39752
0.398155
0.3989
0.398953
0.39953
0.40001
0.4005
0.40195
0.40303
0.40474
0.404814
0.4068
0.40703
0.4076
0.40799

0.408065
0.409135
0.41027
0.41029
0.41048
0.410723
0.41075
0.41077
0.4111
0.411491
0.41205
0.41205
0.4123
0.41353
0.413713
0.4145
0.4148
0.4148
0.41483
0.4157
0.41657
0.417633
0.41844
0.42009
0.42065
0.422598
0.423722
0.4244
0.42455
0.4256
0.42668
0.42725
0.427355
0.427874
0.4284
0.4291
0.4295
0.42993
0.43008
0.432493
0.432999
0.433741
0.43413
0.434388

0.4344
0.4347
0.4369
0.437575
0.43843
0.4385
0.439895
0.44085
0.4428
0.4432
0.443555
0.4438
0.4438
0.44396
0.4455
0.44568
0.44572
0.44602
0.44745
0.4476
0.4484
0.4487
0.450761
0.4514
0.451481
0.45163
0.4522
0.4542
0.4542
0.4544
0.45495
0.45605
0.4575
0.4576
0.45761
0.460923
0.46125
0.4619
0.462
0.46224
0.463365
0.4636
0.4639
0.4672

0.4675
0.46861
0.46937
0.46963
0.4698
0.46985
0.4701
0.47039
0.4705
0.4713
0.4714
0.4727
0.4743
0.474625
0.47775
0.4811
0.48166
0.4843
0.485
0.487021
0.48706
0.48775
0.48924
0.48948
0.48973
0.49
0.49026
0.49034
0.490368
0.49129
0.49189
0.4923
0.49308
0.4949
0.4955
0.497084
0.49737
0.49737
0.4978
0.49781
0.4984
0.4987
0.49888
0.4993

0.5001
0.503004
0.5031
0.5035
0.5042
0.5061
0.50643
0.5069
0.507188
0.50727
0.5082
0.50915
0.5094
0.51373
0.513997
0.5146
0.51625
0.5211
0.5213
0.5224
0.523
0.5243
0.5243
0.524835
0.52541
0.5264
0.5286
0.528788
0.5308
0.531016
0.5314
0.53161
0.5325
0.5332
0.5359
0.537261
0.53765
0.53779
0.53862
0.5391
0.53929
0.5418
0.5427
0.54393

0.54393
0.54427
0.54575
0.546557
0.54717
0.55001
0.5505
0.5507
0.55108
0.5525
0.55292
0.55302
0.5542
0.55494
0.5552
0.55523
0.55687
0.55704
0.55837
0.55924
0.56188
0.5621
0.563
0.565
0.56758
0.56787
0.56836
0.56991
0.570937
0.572
0.5725
0.5732
0.57332
0.5738
0.5741
0.57497
0.57507
0.5751
0.57597
0.577
0.57875
0.5794
0.58051
0.5813

0.5817
0.58207
0.58289
0.58455
0.5849
0.58546
0.5859
0.5863
0.5872
0.5876
0.58828
0.58935
0.5896
0.59088
0.59096
0.591097
0.5912
0.593
0.5936
0.5945
0.5948
0.596
0.5967
0.5971
0.5977
0.59799
0.598
0.5983
0.5983
0.59947
0.5996
0.600597
0.60272
0.6027275
0.603
0.6036
0.6036
0.604
0.6059
0.606713
0.6069
0.6071
0.608185
0.6095

0.6095
0.61033
0.61202
0.61283
0.61373
0.61392
0.61422
0.6158
0.6158
0.6169
0.6171
0.6174
0.6179
0.61812
0.61828
0.61921
0.6193
0.619303
0.62
0.62003
0.6201
0.6202
0.6203
0.6206
0.62104
0.621771
0.622
0.622751
0.6244
0.62478
0.62478
0.6256
0.6287
0.6305
0.63223
0.63234
0.63239
0.63279
0.63315
0.6348
0.6355
0.63575
0.63595
0.6362

0.6365
0.6365
0.636989
0.6377
0.6378
0.63866
0.6397
0.63999
0.642719
0.643
0.64582
0.6458537
0.64594
0.64629
0.64932
0.64985
0.6518
0.65205
0.6526
0.6527
0.6528
0.65425
0.654432
0.65488
0.65559
0.65609
0.65621
0.6563
0.65755
0.65755
0.65886
0.66155
0.661657
0.6624
0.66249
0.6635
0.6644
0.664571
0.66458
0.6658
0.6661
0.6663
0.6682
0.6685

0.6685
0.6687
0.6692
0.67012
0.6708
0.67099
0.67128
0.671441
0.67405
0.6744
0.67459
0.675
0.6755
0.67636
0.677
0.6776
0.6783
0.67922
0.68052
0.682
0.6826
0.68282
0.68316
0.684
0.6846
0.6852
0.6859
0.687502
0.6896
0.69013
0.69081
0.6932
0.6933
0.6941
0.6948
0.695
0.69694
0.697
0.6978
0.69862
0.700856
0.701
0.7011
0.7018

0.70368
0.70424
0.7068
0.707
0.7071
0.70746
0.70792
0.70925
0.70932
0.70959
0.70986
0.712
0.7134
0.713781
0.71471
0.71692
0.71772
0.718
0.719
0.719
0.7203
0.7205
0.7205
0.721929
0.7227842
0.722911
0.72347
0.724199
0.7243
0.7279
0.7285
0.7298
0.72987
0.73152
0.733
0.73574
0.73574
0.73612
0.7365
0.73827
0.73934
0.7395
0.7408
0.7421

0.7474
0.7508
0.7508
0.751637
0.75261
0.7527
0.75282
0.7546
0.755
0.7564
0.7564
0.756729
0.7585
0.7605
0.76177
0.7626
0.76269
0.76269
0.7636
0.7638
0.7658
0.765807
0.76647
0.76729
0.7677
0.76856
0.7691
0.76915
0.7694
0.77276
0.7752
0.777921
0.778
0.7794
0.78414
0.7851
0.78523
0.78548
0.78616
0.7869
0.7874
0.790711
0.79107
0.7929

0.7955
0.79574
0.79771
0.79773
0.80028
0.80365
0.80584
0.8059
0.80634
0.8072
0.8079
0.80811
0.8084
0.80998
0.81177
0.8118
0.81263
0.81292
0.8137
0.81417
0.815772
0.816
0.81664
0.8168
0.8177
0.8177
0.818514
0.82
0.82036
0.82061
0.8213
0.8213
0.82198
0.82245
0.82248
0.822972
0.83053
0.8325
0.8334
0.83513
0.83555
0.83652
0.836804
0.839

0.8404
0.8409
0.84116
0.84378
0.84591
0.8469
0.84865
0.85198
0.8562
0.8567
0.8569
0.85836
0.85946
0.8598
0.8612
0.86505
0.8651
0.8658
0.867
0.86701
0.867846
0.87239
0.87585
0.8777
0.8782
0.8792
0.88046
0.88198
0.88368
0.8876
0.8905
0.891
0.89147
0.8934
0.8941
0.89858
0.8996
0.9035
0.90362
0.9071
0.90764
0.90896
0.912
0.91555

0.9164
0.9187
0.91955
0.925189
0.9261
0.9282
0.9288
0.9302
0.93424
0.93463
0.93782
0.9403
0.94421
0.94435
0.94746
0.94872
0.95099
0.95278
0.9528
0.95341
0.954
0.9556
0.9569
0.9576
0.9596
0.9597
0.9603
0.9605
0.960754
0.961
0.9614
0.9644
0.968199
0.96837
0.96944
0.96983
0.972
0.9726
0.97623
0.9797
0.9846
0.98569
0.98644
0.9869

0.987
0.9893
0.9927
0.9929
0.99509
0.99638
1.001343
1.00285
1.0057
1.01187
1.0122
1.0143
1.017
1.0173
1.0174
1.01747
1.0185
1.021
1.02739
1.03023
1.03122
1.0348
1.0349
1.037
1.03876
1.04044
1.04505
1.045128
1.04678
1.048073
1.05157
1.0538
1.0562
1.0573
1.059
1.0596
1.06006
1.06022
1.0616
1.06241
1.0639
1.06514
1.0671
1.076

1.077
1.07916
1.0827
1.0854
1.08632
1.0877
1.08864
1.08915
1.093
1.094
1.09686
1.0972
1.1005
1.101
1.10158
1.1018
1.10325
1.1114
1.11553
1.11578
1.124
1.12947
1.131511
1.133
1.1375
1.14051
1.1511
1.15123
1.152
1.15367
1.15408
1.156
1.1599
1.16058
1.16384
1.1642
1.16738
1.16904
1.16912
1.17258
1.1733
1.17706
1.18123
1.18615

1.192
1.1987
1.20477
1.2084
1.209
1.213
1.21538
1.2205
1.22088
1.222
1.2256
1.2295
1.23071
1.235362
1.2388
1.24047
1.24242
1.25189
1.2548
1.2548
1.25803
1.25935
1.260409
1.2609
1.26313
1.27743
1.3013
1.3035
1.305
1.31577
1.32126
1.3216
1.32448
1.325508
1.3348
1.33744
1.34
1.3401
1.34366
1.349
1.34942
1.355175
1.3572
1.358

1.36641
1.36789
1.36816
1.3688
1.37611
1.37706
1.382
1.38519
1.404
1.4052
1.4197
1.436561
1.4412
1.4418
1.44506
1.44835
1.45756
1.4761
1.4762
1.4839
1.488888
1.50279
1.52199
1.52618
1.53809
1.5437
1.5513
1.5573
1.5658
1.56641
1.571
1.57978
1.582
1.5914
1.59621
1.6153
1.6224
1.62629
1.678027
1.6821
1.690975
1.6981
1.706459
1.7087

1.7203
1.72136
1.7356
1.7654
1.791196
1.80669
1.809
1.8296
1.83069
1.8453
1.85151
1.85742
1.87703
1.87729
1.889884
1.9135
1.91882
1.92462
1.9273
1.93771
1.94634
1.947
1.94849
1.96595
1.9825
2.002134
2.02665
2.03251
2.0393
2.04588
2.0786
2.0832
2.090936
2.0977
2.0991
2.10808
2.1124
2.113
2.11649
2.1213
2.1515
2.17086
2.1721
2.18091

2.18261
2.18624
2.18671
2.1894
2.201002
2.20538
2.21183
2.227
2.255457
2.2555
2.2598
2.2699
2.275748
2.2833
2.2934
2.29371
2.301
2.318968
2.3231
2.3443
2.34788
2.3612
2.40865
2.4544
2.4641
2.46607
2.4771
2.5214
2.54734
2.682
2.69368
2.808
2.89961
3.11851
3.3204

SP1 D

0
1.45148E+13
1.23223E+14
1087245
1.47695E+13
173214020
17401248
1.28058E+13

5.6109E+14
112.13664
1.05876E+14
1732140200
11923731000
945128000
6417280000
16614406
210634340
3211185.6
1.01843E+13
254856
16310784
2.2331E+11
2.30809E+14
3.14325E+14
11170536800
1812075
6.48473E+15
205221.24
4948.2209
250983580
3127536
1.68158E+13
3.7444E+12
7232427
8.0902E+12
2.0646E+11
1.42287E+12
9930060
2.09328E+13
276536.224
6.84139E+12
1.85004E+15
4.81155E+12
5864130
11728260
156043.8
5.14093E+11
1274280
3.10445E+12
4.5991E+11
1.38095E+15
47015234000

699832.8
13288.55
54851.76
52960.32
137748.78
1.38095E+15
7894912
1.83983E+16
4.39797E+13
3909420
25629012
6.75435E+12
257950.68
4.37968E+13
1.8722E+12
186306.84
195471
1.55619E+11
2932065
3.33215E+13
1068663.6
47113.95
1.38095E+15
5.0989E+13
2.97965E+16
2368436600
18347560000
4.46264E+15
5.90109E+12
39945274000
1.66563E+12
1.37033E+16
96348000
1.55384E+13
43500160000
724.83
4.9255E+13
13337390000
1449.66
2.07133E+14
2.28095E+12
24466176
7818840
1.17075E+12

1.65829E+14
4.4972E+14
43503.12
2.73639E+14
3.50561E+12
155098.08
9.77288E+14
1.04281E+11
283716
104029.2
1.20268E+13
3.89048E+14
1.11835E+14
1.22884E+11
1449.66
21501810
12628470000
1328.855
11728260
2.79954E+13
0
4.83032E+13
1.80116E+12
387745.2
133346.52
6.62537E+13
2.54619E+13
5.36466E+13
9.32459E+15
233988000
1.22424E+13
1.484E+13
1842822000
5302470000
3.79103E+12
1497982
1.08524E+12
22682184
94296720
16912.7
6.37362E+13
2.95054E+12
1.41228E+13
1.33961E+13

8386.235
12901.9
1891.44
28371.6
5.51971E+15
1.42768E+12
8.0902E+12
78188400
72483
99063800000
37139490
16810506
20805.84
6.84145E+11
2948900000
5.97609E+11
6.78627E+13
75657.6
8.56609E+13
1.38009E+13
1153778.4
9198200000
7.4888E+11
6.04385E+14
2.85536E+12
3.04572E+14
8.49816E+12
7.6143E+12
8.27853E+11
217515.6
2.39044E+15
8.32815E+14
7.49416E+11
2.88937E+17
6402.665
5.20512E+14
8214.74
301025340
3.4932E+13
2.04634E+13
1.53691E+11
47715200
2.1342E+15
33554.19

2.44335E+13
1.33609E+13
2.30809E+12
3.46024E+11
1258251.6
7.40455E+12
7.31594E+11
435031.2
314.093
13682970
564594.84
2.40404E+15
3.60232E+11
12112320000
19328.8
19251840000
2.80545E+13
9457.2
20805.84
5082246
7.91356E+13
71722.872
414523950
2.14152E+13
2837.16
2.29204E+13
0
18914.4
1.06227E+14
57688.92
7.41196E+11
2.90295E+12
1.42768E+12
67146.12
5967493.2
1.0807E+11
1.33725E+15
13246
1.59424E+13
10268.425
7.44898E+13
5.04325E+11
9.29018E+13
41292000

2.07627E+14
4.83032E+12
8093.935
9.75583E+11
2345652
9.75583E+12
13282112000
6.42457E+12
1.18974E+14
1.10653E+13
1.96097E+14
604.025
7.96397E+15
43003620
30263.04
977355
5.09207E+13
2.37947E+12
51946.15
16360.956
2142362160
267638.76
8.72618E+15
1838189600
112540.68
3.64059E+13
16017300
1.28491E+13
4.12004E+14
2092720000
14855796
132460
28026.76
9.06441E+11
4.2082E+12
604.025
5.93517E+12
11114.06
5.94868E+12
3.52162E+13
945.72
1.50344E+15
2.16139E+11
3.33007E+13

5674.32
17317184000
2.96352E+12
65702380
1.61953E+13
116323.56
7.65493E+11
2.09671E+13
3865.76
1.93917E+13
2.86064E+15
2.09393E+14
992992680
3.67272E+13
3.68818E+14
72046400000
2.48101E+12
2.40595E+14
6.01143E+13
1.80586E+14
50536080000
2.70788E+11
1.97496E+15
2742.588
2.18911E+14
8818.765
2416.1
242061400
5.30802E+11
104029.2
33450072000
0
8854840000
6.45739E+12
1954710
2.02574E+13
2931.732
2174.49
3.16113E+11
2.04634E+14
7.3186E+12
9.04199E+14
5.52847E+12
1559920000

62417.52
2416.1
1.0554E+16
8.60439E+14
66460140
2.33077E+13
4.55705E+13
11180941200
4.28305E+13
362.415
2.6347E+11
10402.92
78494.76
26284800
27741120000
3020.125
1.76081E+12
5919.445
123146730
22228.12
6.42457E+12
101192.04
4.03592E+13
2416.1
6.39926E+13
43634.1
6.62145E+12
591852000
8209782
1.24415E+12
483.22
6.24264E+13
5315.42
2.09393E+14
211108680
579.864
3538680000
538114.68
4.4286E+12
53913440000
14635720000
3.11711E+13
979309710
2.14152E+12

8.56609E+12
1.76081E+12
2.74226E+15
11424120000
5.9476E+11
2615900000
1.32385E+12
4.11648E+14
1.44093E+11
1932.88
2064600000
3.63296E+16
22588500
5.40348E+11
18724.775
5436.225
5277717
2.14152E+12
945.72
3.39355E+15
23456520
2.74226E+12
241.61
29446080000
7272202000
2.8958E+13
14280.372
2.97436E+15
3.33215E+11
8.0902E+13
5.41758E+15
1.18974E+13
6056160000
1.07936E+17
1.143E+17
1563768
5.47278E+12
4.6734E+14
1691.27
5.22076E+15
65522560000
2.45085E+14
2.09393E+13
116.1171

5668659
58548800000
2.65172E+12
2.92945E+13
2.2367E+13
3.80715E+13
4.52099E+13
1.23732E+14
13618.368
7610.715
1.35087E+11
9.04199E+14
14660325
1.77955E+12
6.60359E+13
6903.756
77400300000
4.40485E+12
23926.716
4823.172
5.88578E+12
7.84407E+12
2.18219E+12
72046400000
10359963
4.28305E+12
5.62359E+13
6.90046E+12
604.025
6809.184
6.87157E+12
4.68198E+17
2.14152E+12
3.96255E+11
4.0213E+13
66533400
1.1685E+15
2.15906E+12
4.46009E+13
1.55384E+13
75657.6
773.152
1.3325E+14
22100100000

22100100000
2.61742E+12
821.474
1.54678E+15
3.91075E+12
25534.44
3.56807E+14
1513.152
1172826
7.43303E+13
9.20986E+13
2.43101E+11
1.59424E+13
1.1835E+12
8.17948E+14
1.01868E+13
8.12365E+12
8209782
1.61804E+15
1.58271E+14
1368297
3.69238E+11
1.17323E+13
1.52754E+17
1.45148E+13
1.90358E+12
31848120000
3125834000
1.54701E+11
12556320000
241.61
5.52037E+13
1.38993E+14
1986.012
3.01454E+12
1172826
39780180000
977355
340999400
1.25721E+14
2.61742E+11
1796.868
8.39193E+15
1.26285E+15

12818058000
6.59207E+12
8.64557E+11
6.01143E+15
1368297
5.89508E+14
1.97496E+14
35730900
7427898
1.98128E+11
2.61742E+12
3.2338E+11
5.63525E+11
1.08999E+17
3.33126E+12
2.99558E+13
3.80715E+12
36856440000
23543100000
2615900000
47096.856
9.04199E+12
977355
3.33126E+12
96236260000
21955800000
6.42457E+12
5.94868E+12
1.17784E+12
4823.172
6.03389E+11
1.97301E+15
6.20534E+13
1.04694E+12
1.84221E+14
4.27028E+15
1.88345E+13
5.66314E+13
3.98768E+12
5201.46
1.92737E+13
34925040000
8.56609E+12
4.0451E+12

1.54701E+11
19890090000
24399.576
1.49907E+13
188108000
1.87978E+12
14637200000
1.69963E+16
12483.504
2.61328E+15
195471
1.00877E+11
632729600
1.58892E+12
2.60268E+13
1.59926E+16
3.85786E+14
4539.456
3.6593E+11
51258.024
19177840000
2.30809E+13
5.5238E+13
1251.4843
50974.308
2.90295E+14
6.19202E+11
4.34087E+11
3.56921E+12
5.61037E+12
2.52224E+13
4.46009E+12
2.49557E+14
1.50727E+12
1.98128E+11
3.23799E+15
3.33126E+12
5.23483E+13
1.57739E+14
116076400
2.14813E+14
3.09401E+12
1.55222E+14
467185.68

7.17493E+13
2.1989E+16
7.38476E+12
1.23014E+13
308025000
105920.64
58978000000
1.15123E+12
2.29204E+12
1.44093E+11
3.29603E+12
5.35381E+15
3.08845E+13
1.76081E+13
62417.52
3.95153E+13
1.76934E+11
1.74525E+12
6.59207E+12
586413
3.15203E+11
5.04448E+14
23643
525820.32
7427898
25874100
9.04199E+12
22865408000
2.18911E+12
3.37885E+13
6.80396E+13
1.40135E+11
2.4014E+14
8.22587E+15
6.06981E+11
5.74603E+11
3.80715E+12
2.52224E+13
1.26285E+11
662.004
977355
9.29322E+11
1.52803E+12
1.14448E+15

3.27613E+11
3.56921E+12
2.70174E+12
6.06981E+11
2.61742E+12
3.62625E+14
11537.784
145706
6409029000
1.67287E+15
2.09847E+15
367040000
84169.08
83223.36
5.0706E+12
3.80715E+12
1.10653E+13
156066000
9.90638E+13
1.38795E+13
6.36678E+13
7.8033E+13
5.23483E+12
18519092000
1.47445E+11
1469648.88
3.80715E+12
2.37947E+12
2.2605E+14
2.34151E+12
1.83242E+13
288444.6
70058760000
4.75894E+12
1452368400
244941.48
6.30406E+11
5.88922E+11
1.92271E+11
10829049000
7427898
9.27002E+13
1.28491E+13
5.63821E+12

1.69963E+13
193872.6
331002
8.87575E+14
1.09871E+12
1.02317E+13
1.1644E+13
1.7212E+14
7.6143E+12
1.18877E+13
5579.748
574980000
1.66563E+12
289044000
4.49887E+14
1.54666E+13
1.12003E+12
2364.3
4.44961E+13
2.11888E+13
1.86239E+15
8533680000
2.40455E+13
3.34769E+12
586413
2.76975E+13
1.57602E+14
1.49907E+13
1.53343E+11
6620.04
2.57243E+13
96259200000
96259200000
9.4572
5.34428E+14
1386425.52
4.49935E+11
4.35809E+11
5231800000
5.8369E+14
5.23483E+12
1.73176E+13
6.84527E+15
1.68327E+12

8.28534E+12
1.3325E+13
115377.84
1.44872E+15
1.67651E+11
1.18974E+13
2.37947E+12
22035.276
1.49907E+13
1.43192E+12
1.36722E+12
945.72
3.80715E+12
4.14285E+13
5.89508E+14
4066.596
4.6257E+14
4.04927E+14
1.0743E+15
53040240000
3.15203E+12
3.51388E+11
1.38095E+14
1.19522E+11
8.87166E+14
1.09509E+13
6.22077E+12
2.37407E+14
3.593E+14
3.5167E+13
7139224000
14131040000
3.41081E+13
5.47278E+12
779508600
4.6257E+11
9.51788E+14
8322.336
3.82007E+13
1.52803E+14
2.7619E+12
195471
4.75894E+12
1.09871E+13

6.90046E+13
179119.368
6.12778E+14
3.33126E+12
8.71061E+12
1.87279E+13
3.33126E+12
52.429
9.04199E+12
1.07076E+12
1.42717E+13
1409.1228
8.73563E+12
2146.7844
1.69963E+13
1.44389E+11
8.56609E+12
4.84493E+11
1.17115E+12
283.716
2.61742E+12
4.5991E+11
205350000
4.12004E+15
4.75724E+12
1.1685E+13
3.31502E+12
4.33193E+13
1.78315E+12
4.28305E+12
4.28305E+12
3.33126E+12
2.43786E+11
9.4572
2.26946E+13
2.2367E+13
97746600
4350.312
1.06227E+13
31284240000
7.25757E+15
255.3444
29679920000
3.02694E+13

1.29487E+14
64232000
58548800000
2.99813E+13
2.69005E+11
5.50089E+15
220224000
8.10522E+11
6.37362E+13
851.148
2.61742E+12
3.33126E+12
8.99662E+15
1.90247E-06
192696000
3.39926E+13
1.14602E+14
1.02675E+11
1.06227E+13
1.10964E+11
4.70862E+14
1.29487E+14
7.37129E+12
178932000
1.992302
8.28571E+12
48884400000
7.2947E+11
1.8873E+11
7.09904E+11
1.11835E+13
31.4574
1.68454E+11
7903052000
4.70862E+13
28743820000
1.12705E+12
4.59238E+13
7.6143E+12
5.93598E+11
5543932000
4.32941E+12
12208446000
22100100000

2.70174E+12
570873000
56.7432
48884400000
1.00431E+14
6.20534E+13
2.59169E+15
5.05361E+12
6.06981E+11
8.0902E+12
2.56691E+12
4.68476E+12
1.12172E+16
1.07076E+13
5.8144E+12
64232000
1.74871E+12
2.68391E+13
691604000
1.83695E+11
1.80116E+11
1.80116E+11
1.01028E+12
71392240000
1.38651E+16
6.55866E+11
77400300000
378.288
3.80715E+12
1.43492E+12
356176060
2.40348E+11
3.15203E+11
3.80715E+12
3.93058E+11
8841742000
3.06197E+11
8.07307E+13
8.5814E+13
6.19202E+12
2.5662E+13
25031240000
4.52099E+12
35360160000

8.39953E+13
1.30584E+12
2.78796E+11
7.57708E+12
1.29882E+13
1.4049E+13
2.11888E+12
1.23732E+13
6.90046E+12
2.49706E+13
35053060000
12834560000
2.78398E+13
2.00116E+14
6.90046E+11
2.50153E+14
4.47319E+12
2.72734E+11
85.1148
5.63821E+12
1.76194E+12
25.16592
1.05901E+11
586.3464
93050560000
2.04634E+12
1.62104E+11
79020160000
141.858
6.79972E+14
36097200000
1.00837E+14
9.10059E+12
4.42002E+11
2.81085E+13
88237600000
1.41391E+12
1.88345E+13
39238500000
2.40326E+12
2.80138E+12
5.24273E+13
37.8288
9.30506E+11

7.06293E+12
1.87978E+13
1607.724
2.14152E+12
1.04281E+11
1.04281E+11
3.49706E+12
189.144
8.15288E+11
1.02675E+11
4.03718E+11
2.61742E+12
2.40648E+11
2.40648E+11
1.92737E+12
2.37947E+12
2.30318E+11
113.4864
4.14267E+11
1.50864E+16
6.41728E+11
6.41728E+11
5.69457E+14
1.05784E+13
94.572
1.44093E+11
6.06981E+12
3.05605E+13
32086400000
32086400000
7.17493E+13
1229.436
247752000
59359840000
5.90176E+12
1891.44
1134.864
2948900000
3.19706E+13
8056972000
4.05246E+12
5.30802E+11
4708620000
64875800000

1.71322E+13
1.67156E+13
4.54581E+13
35386800000
8.73563E+12
1.7196712
416.1168
9.4572
1.26081E+11
8.91574E+11
8101816000
4.14267E+11
3.55501E+13
431645700
65569920000
2364.3
40910160000
3.29603E+12
4.14267E+11
5.17985E+11
3.37885E+14
3.78854E+12
1.77277E+11
1.46811E+14
605.2608
1815.7824
5.22657E+13
4708620000
8227.764
4.44325E+12
3.53602E+11
1.02675E+11
30638220000
14374.944
1.05921E+13
662.004
8.92018E+14
6.82162E+11
6241.752
90610410000
7.29836E+13
123876000
5.73452E+13
2.34099E+14

2175.156
1.66607E+12
1.45438E+14
4.94405E+14
11457642000
17647520000
17647520000
9173.484
5.47278E+12
5.00328E+13
1684536000
119103000
2.2367E+13
3.17749E+11
1.44908E+16
1607.724
5043840000
4.49935E+11
5.21087E+11
37.8288
8.0902E+11
1.0807E+11
8.56609E+13
6.90046E+13
2.06284E+13
0
0
2.14152E+14
82721640000
378.288
94.572
1.44093E+11
19357660000
2.29204E+12
3.69627E+15
3609720000
2.09716
1.07076E+13
1.06654E+14
3.95678E+12
2165832000
6.93447E+11
2.19017E+13
2.07133E+12

24310110000
4.46009E+13
4.23273E+11
1.6025E+14
1.06268E+13
7.40015E+11
2.50153E+14
851.148
18.9144
2294000
1684536000
4.29008E+11
5.21087E+11
6.39412E+11
1.51722E+11
66.2004
5.67365E+11
2.61168E+12
4.47319E+12
482.3172
2406480000
3735.594
8.0902E+13
1283456000
2.11888E+12
1.09283E+11
4.14267E+11
1.27985E+15
3.25987E+13
5585520000
2.19017E+13
1.47953E+12
2.2367E+13
2.14152E+12
9392709000
75.6576
2.43157E+11
9.75583E+14
2648.016
2.61742E+12
1925184000
0
18.9144
2.81471E+11

1.37268E+16
44396670000
3.62422E+13
9.07891E+12
4.40114E+15
1.11359E+16
113.4864
1.98128E+11
34410000
7.64013E+12
2.86121E+14
14593288400
295704000
229992000
1.11835E+14
28.3716
1.78928E+13
1.62104E+11
2.13723E+16
5.47278E+12
193939200
75.6576
6.30406E+11
6.30406E+11
6.90665E+14
2.25145E+12
1.8873E+11
3.04572E+14
15747126000
1.61804E+12
2648.016
662.004
5.42645E+15
2.14152E+12
3609720000
7.04776E+11
9.4572
3.24209E+12
2.97191E+11
18.9144
3369072000
50023260
1.92182E+14
122.9436

132.4008
8.14947E+12
1.46271E+11
2.52224E+13
4728.6
6620.04
2.14152E+14
38605800
7.50586E+15
28730130000
132.4008
82382720000
5.23483E+13
1.50727E+11
2.94754E+14
30807680000
4.57742E+13
6.62145E+12
3051501000
3.38712E+13
18.9144
4.46009E+13
1.38009E+13
3.29659E+14
1.8326E+11
2.43101E+12
1.62104E+11
1.05944E+13
28.3716
7.30906E+13
8.92018E+13
1.3325E+14
6.68087E+12
113.4864
7.94574E+13
1.63084E+13
1.59424E+13
3.64154E+14
1.26285E+11
47.286
1.98128E+11
3.71332E+15
18.9144
6.30406E+11

300632400
4.0451E+13
2.14152E+13
7.29664E+13
3.29603E+12
2.84136E+11
712427600
47.286
0
4.94405E+13
8.0902E+12
9.50304E+12
2.34338E+14
1.34432E+13
0
1.34432E+13
25031240
4.3996E+11
1.36184E+11
1.2973E+16
50438400000
47.286
1.50281E+11
3.49706E+11
122.9436
1.48322E+14
6.59207E+12
6.68631E+13
3.67272E+13
1.54666E+12
92079680000
98157300
3.44662E+11
4.44033E+13
1.97496E+12
1.23336E+13
1.80116E+11
8846700000
3.16081E+11
21232080000
2.2361E+12
8.77289E+14
67251200000
5.88578E+14

2.40326E+13
1.10653E+14
37.8288
2.62566E+15
9.73614E+12
1.07076E+13
6.42457E+11
19890090000
75.6576
2.06284E+13
6.40903E+11
6.42457E+11
5.90109E+12
71051100
28730130000
67251200000
3.31072E+12
1.24778E+14
7.91979E+11
15470070000
9.06104E+12
53800960000
0
4.24289E+14
1.1006E+15
9.75583E+11
6801340000
47075840000
2.40348E+11
3.4222E+11
4.64102E+11
6.64691E+13
47.286
2.88186E+11
2.2361E+12
4.90934E+11
8.32815E+13
8.27841E+13
3.55501E+12
3.54412E+11
2.30809E+13
6278160000
28.3716
3.31072E+12

28.3716
2615900000
1.49907E+13
5.81751E+13
2.43786E+12
1.67384E+14
2.52192E+11
2.90876E+14
1.11835E+12
7770444000
18.9144
4.94405E+14
6.22074E+11
1.72586E+15
2.3464E+15
343345200
28.3716
2.44848E+12
1.28783E+12
2.64291E+12
18.9144
1.67156E+12
35576240000
28.3716
2.07359E+12
2.90876E+14
2.70174E+11
9.69067E+12
1.91767E+14
18.9144
5.21197E+11
8.56609E+11
3.31072E+12
1.07478E+12
2.14371E+11
7.07203E+11
7.53379E+13
1.41228E+11
65702380
2.15204E+11
1071986200
5.11889E+13
5231800000
9417240000

89107840000
1.53194E+16
8.4064E+11
3.98768E+12
7560987000
3.05605E+13
5.85488E+13
2.25145E+11
20124300
1.9029E+12
47.286
41990190000
6.35664E+12
2.43157E+11
9.27002E+13
2668218000
2.08088E+13
4708620000
8.23827E+12
2.21001E+13
5.71635E+11
16875907200
7.73389E+12
1.88345E+12
1.10653E+12
156066000
2.65201E+12
20748120000
1.0166E+13
86190390000
7.76922E+11
1.72586E+14
3.66866E+12
2766416
2053500000
3.12206E+15
70613760000
1.05688E+15
30940140000
1.7111E+11
84064000000
7.0198E+15
2.26973E+11
4.38252E+16

3.12132E+12
6409029000
4.75802E+11
64090290000
2.43101E+11
2.71484E+12
1.14327E+13
7.90202E+12
2.20248E+11
1.99735E+14
6.1121E+12
68510310000
1.09283E+11
4.14267E+11
1.70647E+15
4.4722E+11
1.78928E+12
3.97802E+11
7953446
10028258
19890090000
4.16124E+11
35360160000
2.03174E+13
17680080000
1.43613E+12
12504002000
1.67156E+13
31944320000
5.96703E+11
4.33193E+12
8.33843E+13
1.34196E+12
1.34502E+13
1.46372E+13
4.47319E+11
1.74525E+15
1.10964E+13
4.56736E+12
7.75668E+12
7.75668E+12
1.59722E+11
68510310000
5.56542E+16

1729010
170440500
4.8589E+12
141691500
6.69929E+12
22100100000
1.27985E+14
4.77925E+13
36593000000
4.0238E+12
6521916000
6.20534E+13
26280952
1.11359E+11
7.84387E+12
1.49316E+14
41990190000
1.30391E+11
4283601000
5.65034E+11
2.08088E+12
2.63961E+12
1.18289E+15
10772661000
2.14371E+11
1991895000
1.34196E+13
9.93217E+11
258741000
1.54701E+12
9.41091E+12
1.0829E+12
5018754000
1.43613E+12
3.29659E+13
1359417000
6.20534E+14
1.68708E+16
1778812000
1464904000
3.97802E+11
2772225000
2.0943E+15
7.17493E+13

1687977000
73186000000
5.04184E+13
10977900000
9061041000
57498000
2.50153E+15
2.11888E+11
1560660000
13260060000
55250250000
1.5217E+16
2.58571E+11
168797700
77338880000
1.8616E+16
4.57308E+11
1.96274E+11
1.78928E+13
7.9506E+15
1.10653E+11
392218500
7.76922E+12
64090290000
44731890000
1.49704E+16
3.31502E+11
56503440000
1.88345E+11
1.12472E+15
1.1635E+13
26695500
4.03507E+11
2.53873E+12
6.53979E+12
1.63541E+11
41990190000
224652900
2.13739E+12
5.73994E+14
3.26168E+12
2.77411E+11
22100100000
1.22168E+14

6.55699E+12
7072032000
4.19902E+12
5.54822E+12
2.20248E+11
264901500
1.68708E+15
86247000
1.83433E+12
22629570000
6.38886E+12
188511300
178654500
1.33803E+14
4199019000
1.91666E+11
7902016000
4.26617E+13
53800960000
8624700
3.59794E+12
174958200
38311.28
5.88448E+12
2.52092E+13
86190390000
1.47953E+12
1.64765E+11
4199019000
1.18289E+15
10087680000
19166592000
1.73172E+12
3.97802E+11
33266700
37660672000
131834700
17485312000
49257360
10062150
6725120000
1.35581E+14
28245504000
1.8616E+15

6160500
 1.81838E+12
 1.3962E+14
 2.71484E+12
 5.51894E+14
 1.61102E+13
 6817620
 12321000
 6037290
 1.06551E+13
 3.95577E+12
 6.06127E+11
 SB2 -31 5
 SI3 0 3
 SP3 -21 2
 c ccccccccc Pulse Height Tally ccccccccccccccccccccccccccccccccc
 F8:P 1
 E8 0.0 1000I 2.0
 FT8 GEB 0.002794 0.0004123 1.402
 c ccccccccc Germanium ccc
 M1 32000 1.0 \$ Germanium
 c ccccccccc SOURCE ccc
 M2 8000 0.670604 \$ Non-Contaminated Soil Earth, U.S. Average
 11000 0.005578
 12000 0.011432
 13000 0.053073
 14000 0.201665
 19000 0.007653
 20000 0.026664
 22000 0.002009
 25000 0.000272
 26000 0.021050
 M3 13027 1 \$ Aluminum Window
 M4 6000 0.000150 \$ Air (Dry, Near Sea Level)
 7000 0.784431
 8000 0.210748
 18000 0.004671
 NPS 1E8